GTT-Technologies
Kaiserstraße 103
52134 Herzogenrath, Germany
Phone: +49-(0)2407-59533
Fax: +49-(0)2407-59661
E-mail: info@gtt-technologies.de

GTOx
Version 19
Summary & Examples

Table of contents

Introduction

The GTOx database Version 19 contains thermodynamic data covering binary, ternary and quaternary sub-systems of Oxides-Metals-Phosphates-Sulfides-Sulfates-Carbonates-Chlorides-Fluorides based on the 26 elements:

Al-C-Ca-Cl-Co-Cr-Cu-F-Fe-H-K-Li-Mg-Mn-N-Na-Ni-O-P-Pb-S-Si-Sr-Ti-V-Zn

with a focus on oxides. Information concerning the sub-systems already assessed in the database is given in appropriate charts in the next chapter. For calculations in higher-order systems the data of the subsystems are extrapolated. The database is the result of an ongoing thermochemical (Gibbs energy) and thermophysical (density, viscosity) assessment project to obtain the data for the respective phases in each system. These assessments have been carried out in the framework of past and ongoing projects sponsored by German as well as European funding agencies in close collaboration with Forschungszentrum Jülich (IEK-2)[1]. A significant database advancement has been made in the last development period with respect to the unification of the thermodynamic description of the liquid state. Details are given in the chapters Phases and What is new in version 19?.

Recently, the scope of the database has been expanded to additionally cover thermophysical properties of oxides. The most relevant properties are the viscosities of slag melts and density predictions. For further information read viscosity modeling and density modeling.

For representative cases of data assessments as well as applications of the data see the Chapters Assessment examples and Application examples. For users with a direct need for phase diagrams calculated using the present database, GTT additionally offers access to its GTOx Documentation, i.e. the full collection of all phases diagrams calculated during the thermodynamic assessments. Please contact us. For those readers who are interested in the recent changes and additions to this version, please check the Chapter: What is new in version 19?.

[1] Forschungszentrum Jülich GmbH - Institut für Energie- und Klimaforschung, Structure and Function of Materials (IEK-2), PD Dr. Michael Müller

Database content overview

The present GTOx database consists of Gibbs energies for the liquid phase (containing metals, oxides, carbonates, sulfides, sulphates, Fluorides, chlorides) as well as 183 solid solution phases and 1366 stoichiometric phases. The Figures (1-5) below indicate systems which have been assessed. Note that an O or R in a blue square indicates that the data are mainly valid for (O)xidizing or (R)educing conditions, respectively.

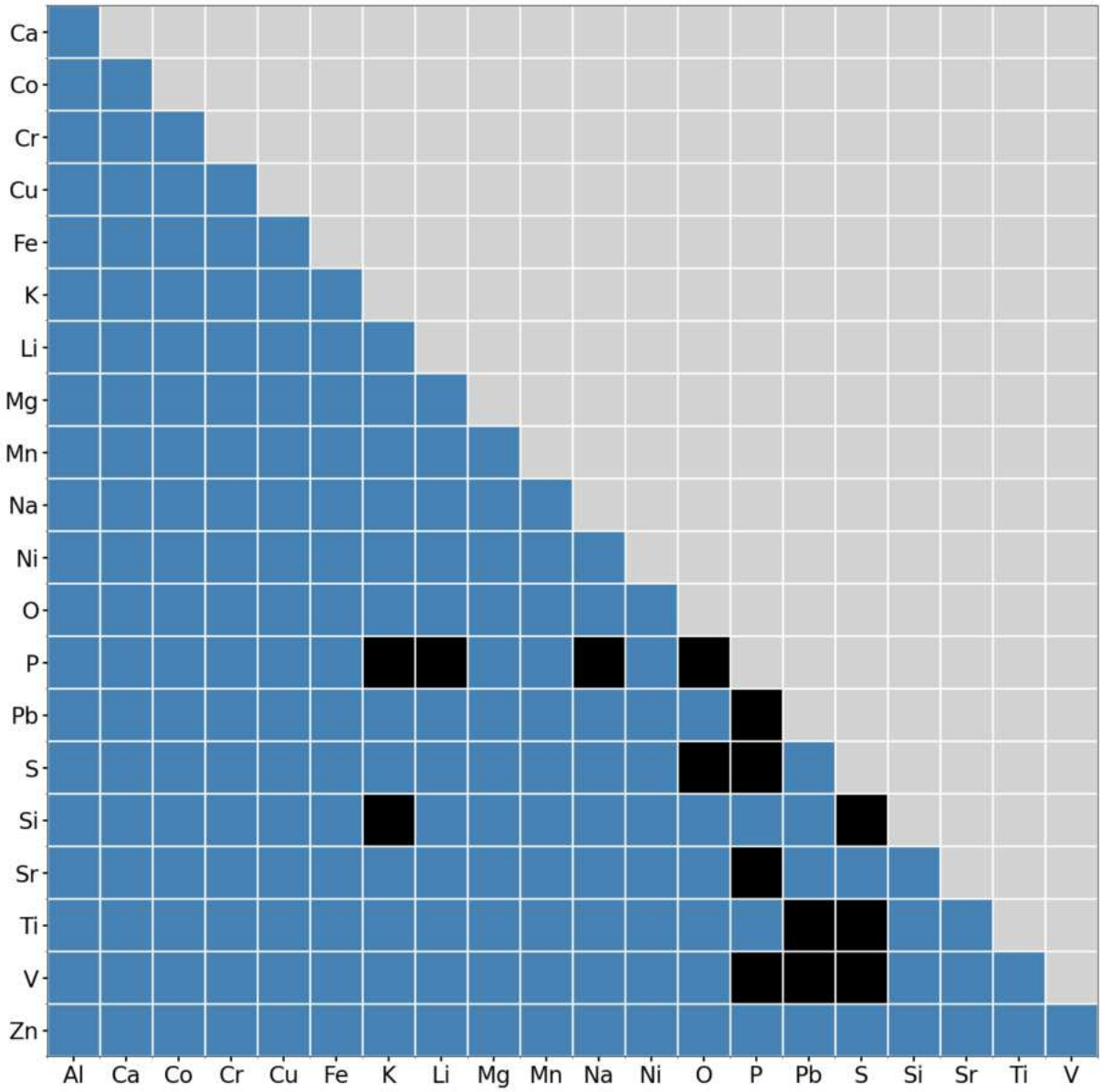

Figure 1: Assessed (blue) binary metal systems in the GTOx database.

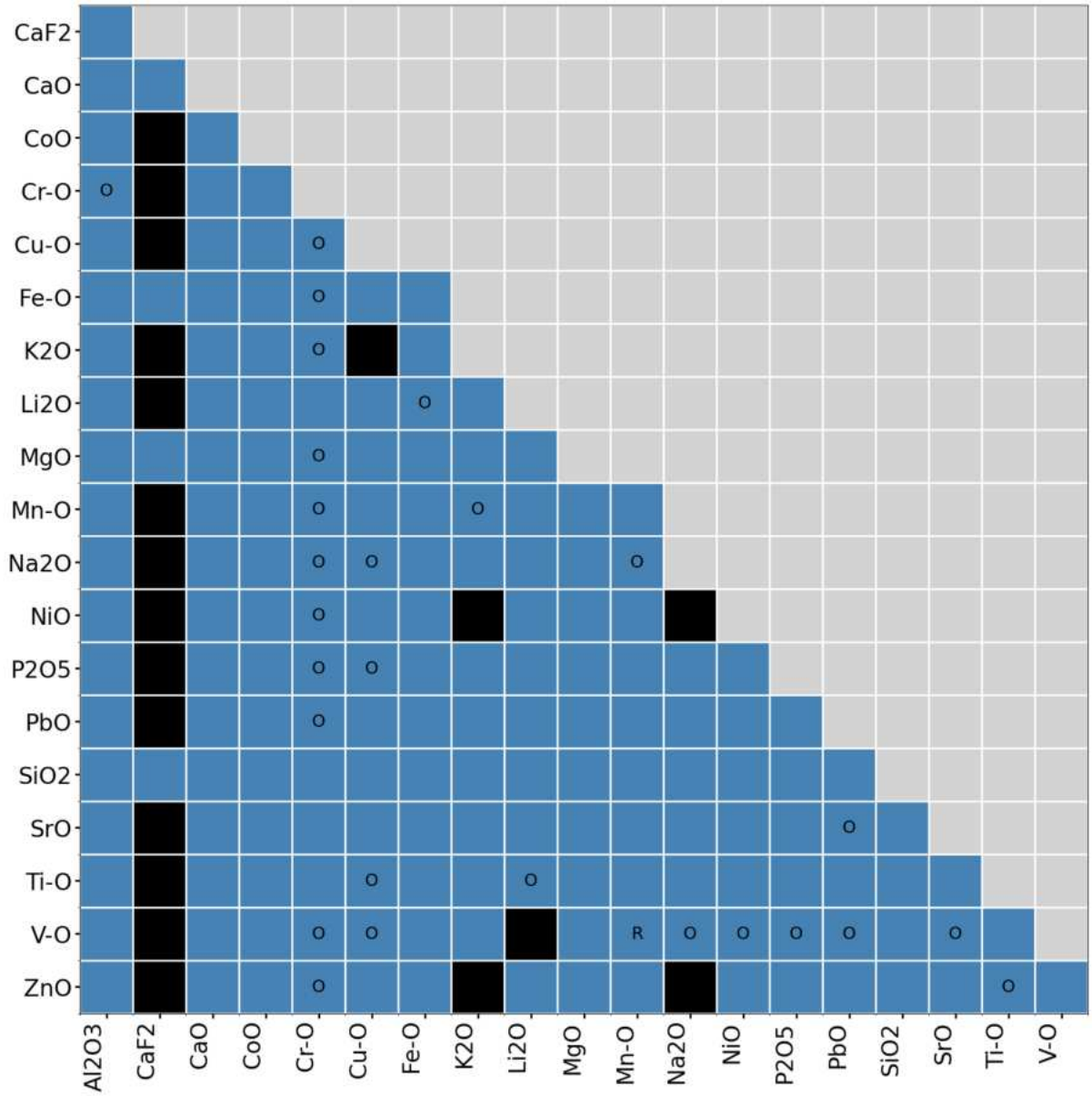

Figure 2: Assessed (blue) binary oxide systems in the GTOx database. O and R denote systems for which the data is mainly valid for oxidizing and reducing conditions, respectively. A distinction is made for metals with multiple valences (Fe, Mn, Cu, Cr, V, Ti).

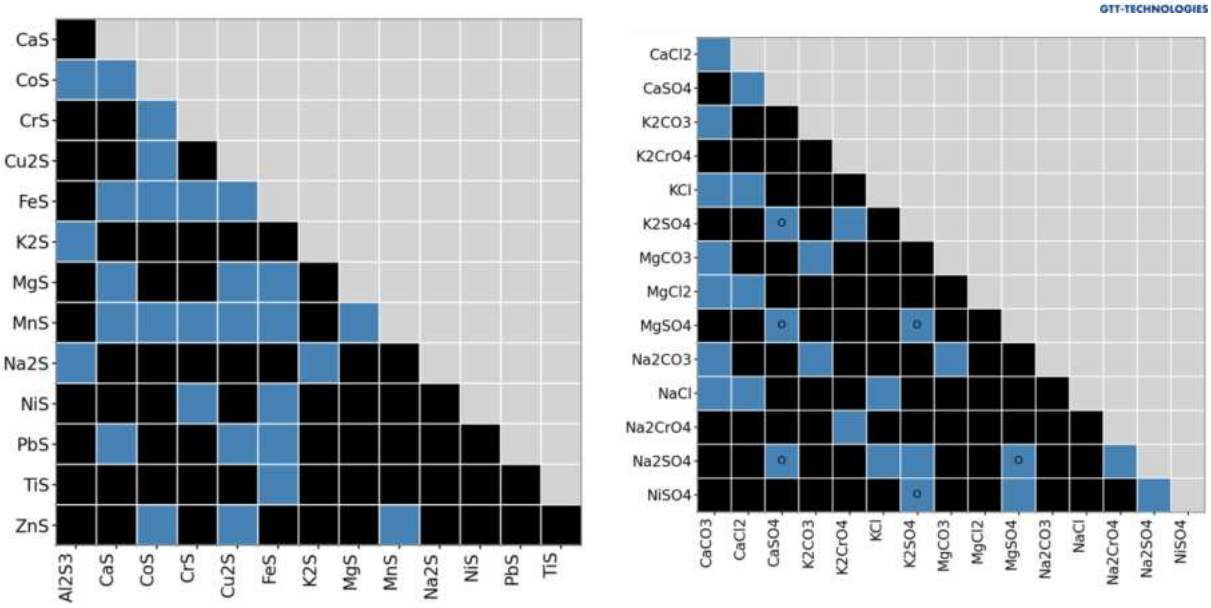

Figure 3: Assessed (blue) sulfide-containing (left) or chlorides-, sulfate and carbonate-containing (right) binary systems in the GTOx database. O denotes systems for which the data is mainly valid for oxidizing conditions.

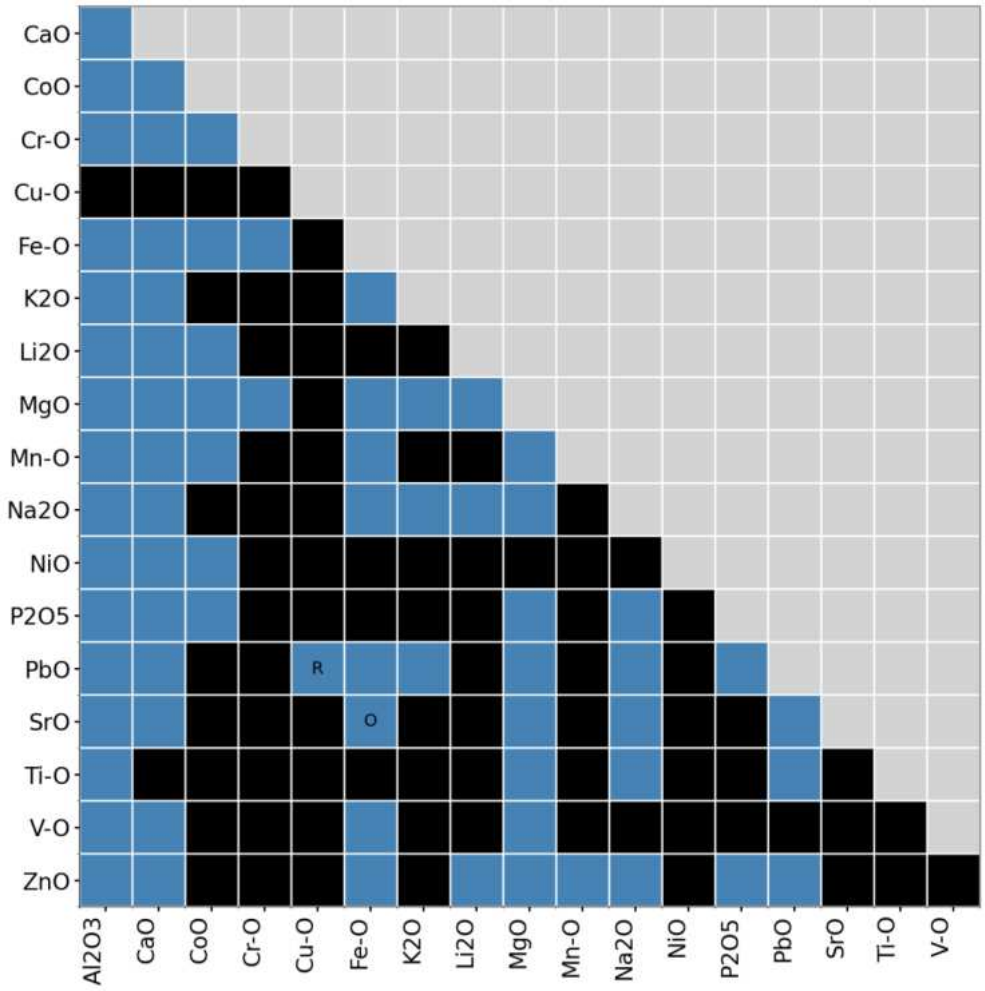

Figure 4: Assessed (blue) SiO_2-containing ternary systems in the GTOx database. O denotes systems for which the data is mainly valid for oxidizing conditions.

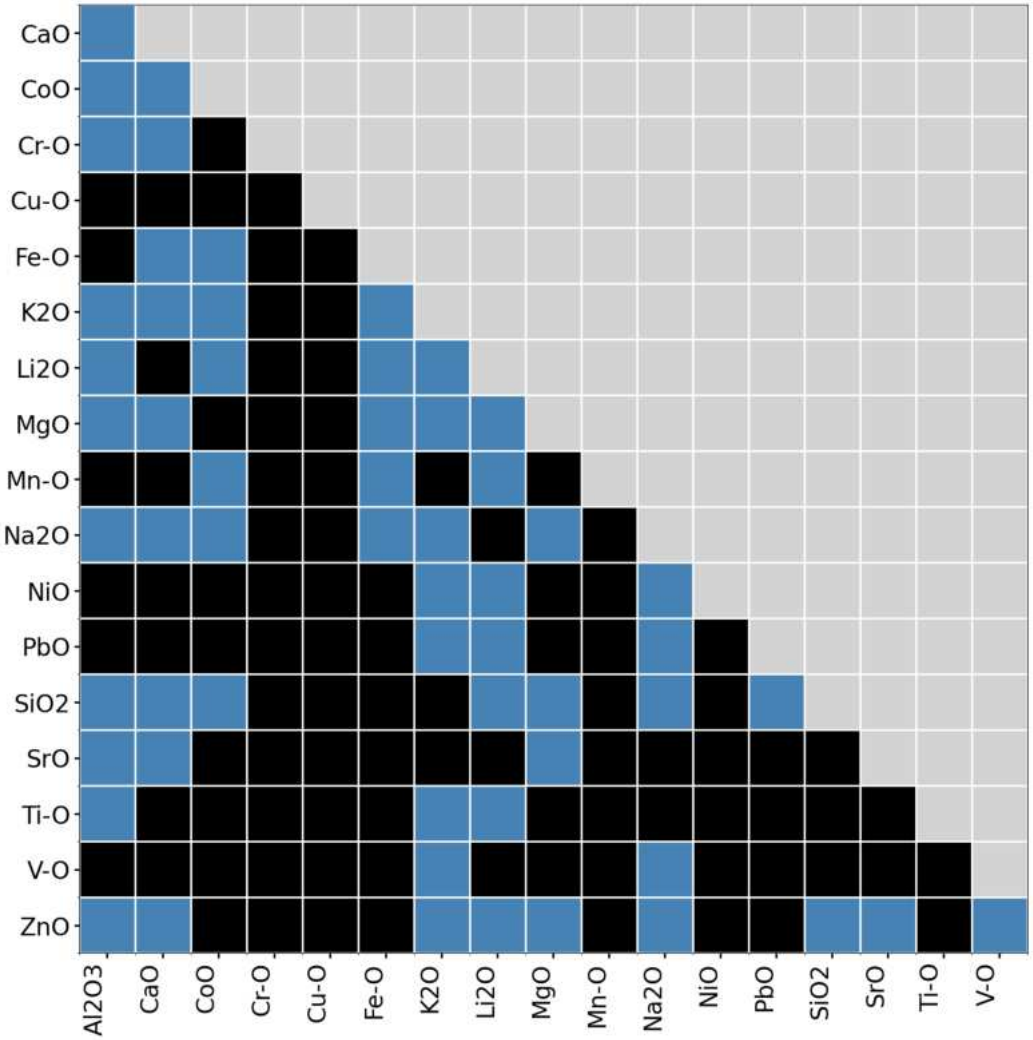

Figure 5: Assessed (blue) P_2O_5-containing ternary systems in the GTOx database.

Figure 4 shows the ternary systems containing SiO_2. As can be seen, most combinations usually observed in ferrous and non-ferrous metallurgy, cement making and combustion ashes (systems with main components from SiO_2-Al_2O_3-CaO-FeO_x-MgO-MnO_x) are covered.

Figure 5 shows the ternary systems containing P_2O_5. Recently, there has been strong interest in P_2O_5-containing systems because of the focus on Phosphorous recovery from, for instance, sewage sludge, but also because many iron ores processed particularly in East Asia contain large amounts of P_2O_5. Furthermore, P_2O_5 is an important component of biomass ashes. To describe these applications, most combinations usually observed – such as systems with main components from SiO_2-Al_2O_3-CaO-FeO_x-K_2O-MgO-Na_2O – are covered.

Thermophysical modelling

Viscosity

A viscosity model for fully liquid (i.e. also supercooled) melts has been developed, where the viscosity is directly correlated to the structure of oxide melts, and the melt structure in turn is described based on the thermodynamic description applied, i.e. using the modified non-ideal associate species model. The present viscosity model covers the system **SiO_2-Al_2O_3-CaO-MgO-Na_2O-K_2O-FeO_x** using a set of model parameters for the viscosity which all have a clear physical meaning.

A corresponding *viscosity calculator* has been developed based on ChemSheet. A screenshot of the user interface is shown below in Figure 6. Note that a valid ChemSheet license is required to use the viscosity calculator.

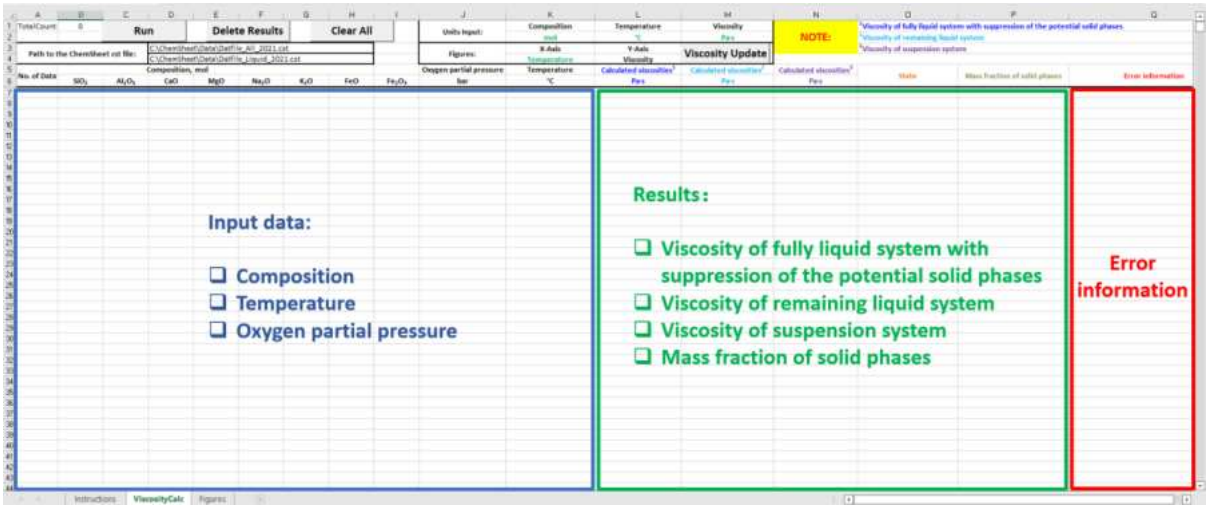

Figure 6: Screenshot of the GTOx-based viscosity calculator in ChemSheet.

Density

A detailed density model for fully liquid (i.e. also supercooled) melts has been developed covering the system **SiO_2-Al_2O_3-CaO-MgO-Na_2O-K_2O**. Apart from that, GTOx utilizes a machine-learning informed density-estimation function to calculate the densities for the remaining multicomponent liquid (SLiq) end members, solid solution phases and solid compounds.

Application examples

Dephosphorisation of steels in the BOF process

In the basic oxygen steelmaking (BOF) process, the accurate control of phosphorous removal up to ultra-low values is very important to ensure a high quality of the product. This has proven to be associated with several challenges, leading to a preferred usage of high-priced low-P iron ores. Thus, in the scope of the European RFCS project BOFdePhos (RFSR-CT-2014-00005), important thermodynamic and kinetic aspects of the dephosphorisation reaction such as the effect of solid phases on phosphorous distribution and lime dissolution in a foamy slag were investigated.

It was found that BOF slags contain solid oxides during a large period of the blow and, in most cases, also at the end of blow. The type and amount of solid phases is strongly affected by temperature and the contents of minority oxides such as MgO, MnO and Al_2O_3. The consideration of solid phases formation in the slag, especially the P-dissolving C_2S-C_3P solid solution, is crucial for a successful modelling and control of dephosphorisation. However, most of the phosphorous distribution equations available in the literature were developed for homogeneous slags. Thus, a new approach for the thermodynamic modelling of the P-distribution between a heterogeneous slag and liquid iron covering the total blowing period in the converter was developed and incorporated in a kinetic dephosphorisation model using SimuSage. The two phase diagrams, depicted in Figure 7, show the most relevant phase relationships pertaining to the dephosphorisation as calculated from the GTOx database.

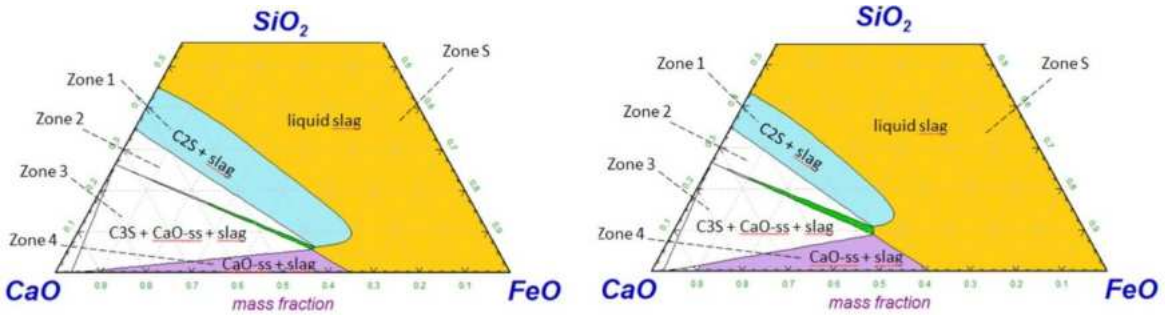

Figure 7: Liquidus isothermals of the system CaO-FeO_x-SiO_2 in equilibrium with liquid Fe at 1550 °C (left) and 1700 °C (right), see also [Khadhraoui2019].

Depending on processing conditions (lime addition, temperature, blow rate, stirring etc.), the actual slag composition mostly varies between the yellow (fully liquid) and light blue (liquid plus C_2S-C_3P) regions. The ranges marked in the diagram are discussed in further detail in the paper [Khadhraoui2018].

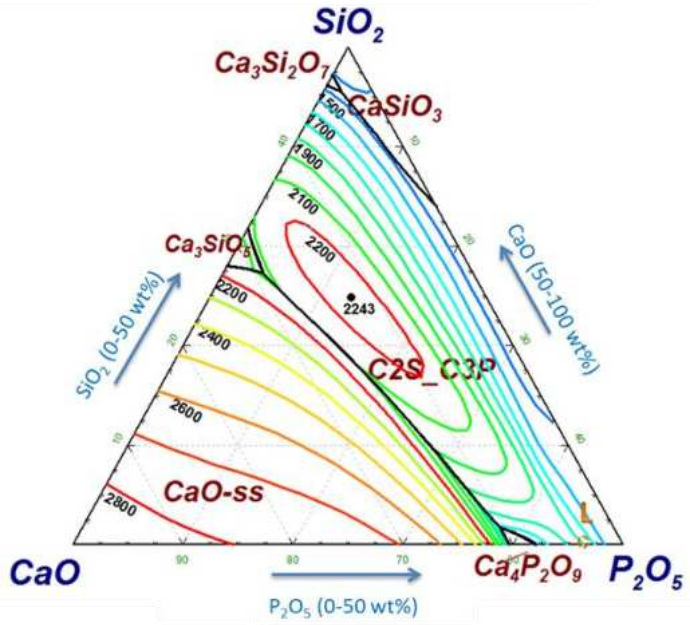

Figure 8: The CaO-rich corner of the $CaO-P_2O_5-SiO_2$ system, see also [Khadhraoui2019]. Note the primary precipitation range of the C_2S-C_3P phase.

Figure 8 shows the liquidus surface in the CaO-rich corner of the $CaO-P_2O_5-SiO_2$ system. It becomes obvious that the very complex pseudo-binary solution phase between the compositions $2CaO \cdot SiO_2$ and $3CaO \cdot P_2O_5$ called C_2S-C_3P is very stable with a congruent melting point at 2243 K. In the BOF process, this behavior leads to the above-mentioned heterogeneous slags, i.e. slags containing both solid and liquid phase contributions. The partitioning of phosphorous between the heterogeneous slag and the steel bath is heavily affected by the presence of the solid silicate phosphate. Using GTOx as the basis of a BOF model enables consideration of this complex interdependence.

References

[Khadhraoui2019] S. Khadhraoui, K. Hack, T. Jantzen, and H. Odenthal, Study of the State of Industrial P_2O_5-Containing Slags Relevant to Steelmaking Processes Based on a New Thermodynamic Database Developed for $CaO–FeO_x–P_2O_5–SiO_2–MnO–MgO–Al_2O_3$ Slags − Part I: Ternary and Lower Order Systems, steel research int. 90 (2019).

[Khadhraoui2018] S. Khadhraoui, H.-J. Odenthal, S. Das, M. Schlautmann, K. Hack, B. Glaser and R. Woolf, A new approach for modelling and control of dephosphorization in BOF converter, La Metallurgia Italiana (2018), n. 11-12, 5-16.

Refractory applications

To improve the lifetime of refractory materials, the potential corrosion by slags needs to be minimized. For this purpose, a counter-cross calculation for the refractory/slag interface is often used [Udagawa1993] [Carlborg2018]. In such a calculation two well specified end compositions are treated like two “components” of a pseudo-binary system. The overall composition of the system is given by the fraction of one of the end compositions. This fraction is changed from 0 to 1 and the resulting equilibrium phase distribution is generated (see below).

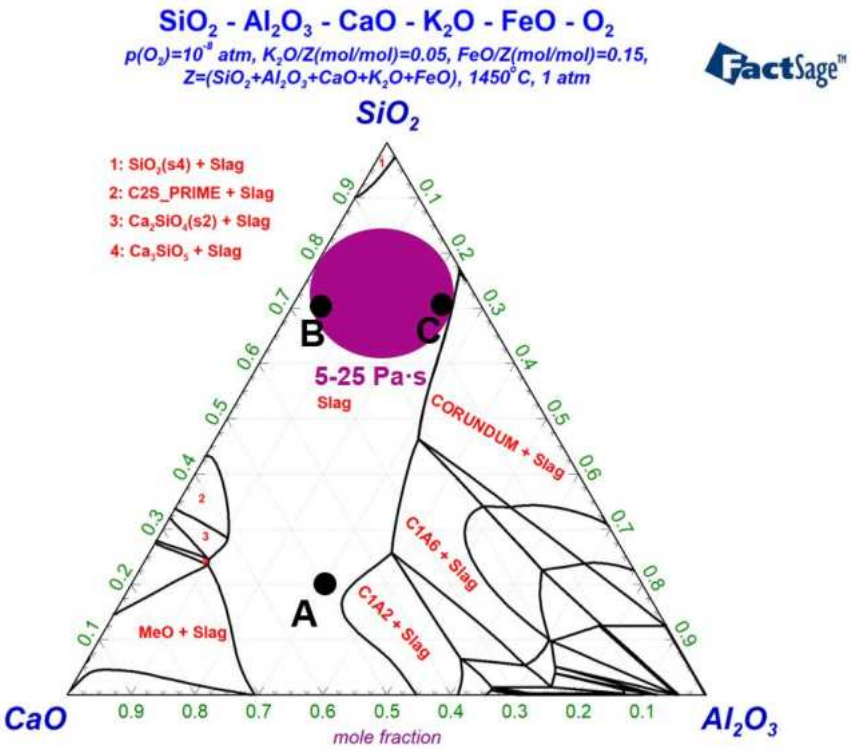

Figure 9: Phase diagram of the system SiO_2-Al_2O_3-CaO-K_2O-FeO at 1450 °C and reducing atmosphere with indicated target viscosity range of 5-25 Pa·s.

The phase diagram of a typical gasifier slag system SiO_2-Al_2O_3-CaO-K_2O-FeO at 1450 °C and under a reducing atmosphere is shown in Figure 9. As an example, a counter-cross reaction between an Al_2O_3-based refractory material (for simplicity pure alumina is used) and a slag with the composition A, marked in Figure 9, is illustrated in Figure 10. Although the refractory can react with the slag A, the formation of three solid solution phases, i.e. $CaO{\cdot}6Al_2O_3$, Kaliophilite-HT, and $CaO{\cdot}2Al_2O_3$ results in the formation of a protective layer on the surface of the refractory. It should be mentioned that in a counter-cross calculation the diffusion rate of each species in both slag and refractory phases is assumed to be the same.

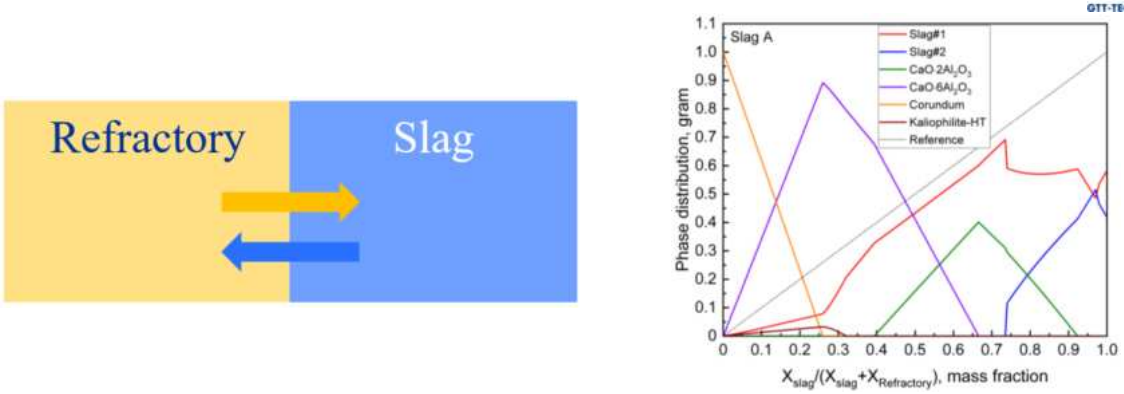

Figure 10: Potential reactions between refractory (Al_2O_3-based) and slag A using a counter-cross calculation.

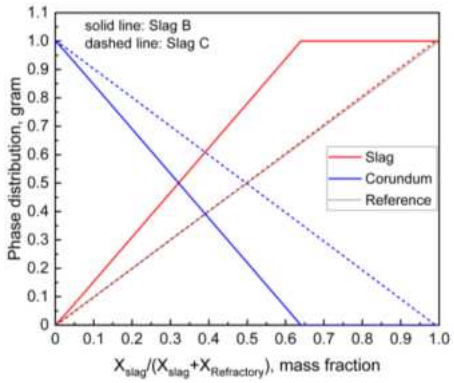

Figure 11: Comparison of the corroding effect of two slags B and C on an Al_2O_3-based refractory material.

Under the constraint that the viscosity range for slags in entrained flow gasifiers is recommended to be in the range of 5–25 Pa·s, the corrosion of the two slag candidates B and C on the Al_2O_3-based refractory material is compared, as shown in Figure 11. Compared to the dotted line as reference (i.e. without any reaction between the slag and the refractory material), an obvious increase in slag mass is noticed for the slag B, which indicates the dissolution of the refractory material into the slag. It will cause a decrease in lifetime of the refractory material. An adjustment of the slag composition from slag B to C can almost eliminate the dissolution.

References

[Udagawa1993] E. Udagawa, E. Maeda, T. Nozaki, Slag penetration into magnesia and alumina monolithic refractories. In Unitecr'1993 Congress. Refractories for the New World Economy. Proc. Conf. Sao Paulo 31 (1993).

[Carlborg2018] M. Carlborg, F. Weiland, C. Ma, R. Backman, I. Landälv, H. Wiinikka, Exposure of refractory materials during high-temperature gasification of a woody biomass and peat mixture, J. Eur. Ceram. Soc. 38 (2018) 777-787.

Distribution of Vanadium

Vanadium oxides were added to the GTOx database because of their important role in ferro-titanium metallurgy as well as in petroleum coke gasification. With the knowledge about the complex behavior of vanadium in slags as well as in liquid-metal alloys it is possible to calculate the vanadium distribution ratios (V)/[V], called L_V, between iron-based melts and slags in a wide range of temperatures and compositions, corroborating the validity of the model under reducing conditions. An example is shown in Figure 12.

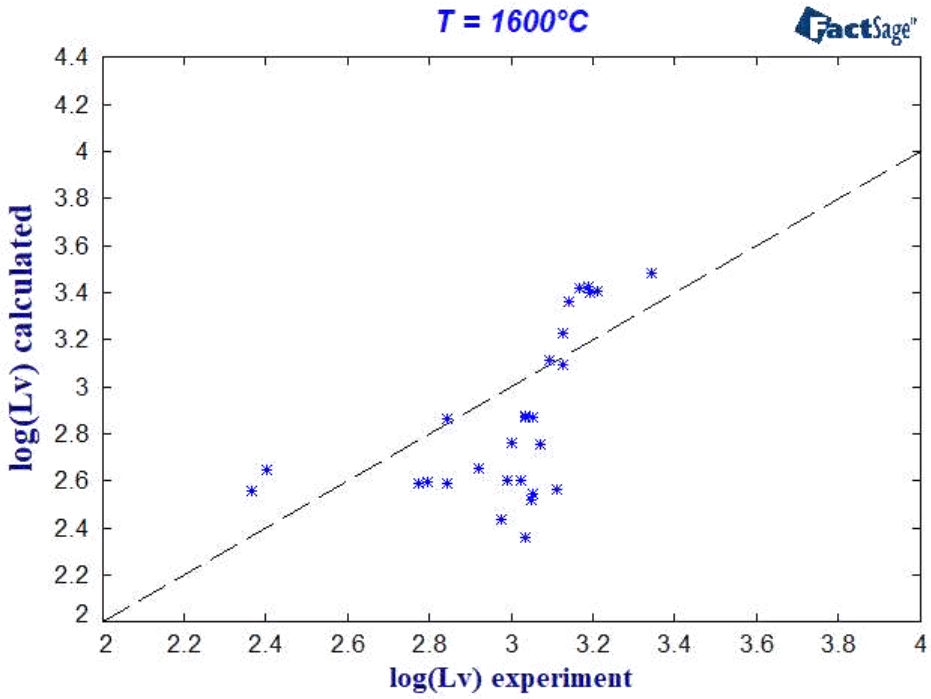

Figure 12: Relationship between the calculated and experimentally determined vanadium distribution at 1600 °C [Inoue1982].

The additionally developed viscosity model shows good agreement between the calculated and experimental values in vanadium-containing slags. More details can be found in the publication by Jantzen et al. [Jantzen2021].

References

[Inoue1982] R. Inoue, H. Suito, Distribution of Vanadium between Liquid Iron and MgO Saturated Slags of the System CaO-MgO-FeO_x-SiO_2, Trans. Iron Steel Inst. Jpn. 22 (1982) 705-714.

[Jantzen2021] T. Jantzen, E. Yazhenskikh, K. Hack, M. to Baben, G. Wu, M. Müller, Addition of V_2O_5 and V_2O_3 to the CaO-FeO-Fe_2O_3-MgO-SiO_2 database for vanadium distribution and viscosity calculation, Calphad 74 (2021) 102284.

Slag formation, fouling, and condensation from coal/biomass/waste gasification and combustion

During gasification and combustion, most of the inorganic species are converted to slag, whereas other inorganic species behave as fly ash entrained in the syngas or flue gas. To understand the slag formation process, ash fusion temperatures (AFTs) are often used in practice. Thermochemical calculations provide insight on AFTs of different fuel ashes with respect to temperature, composition, and atmosphere. Three ash samples from the literature were taken as examples, their compositions and flow temperatures are given in Table 1.

Table 1 Composition and ash fusion temperatures (AFT) of three selected ash samples [Wang2021].

Sample	Composition of ashes, wt%								AFT, °C
	SiO_2	Al_2O_3	CaO	MgO	Na_2O	Fe_2O_3	TiO_2	SO_3	
Ash 1	30.7	27.8	9.21	1.06	0.42	20.6	0.82	8.04	1340
Ash 2	41.5	36.5	7.12	0.56	0.18	8.32	1.33	2.67	1465
Ash 3	44.8	36.3	5.49	0.85	0.34	4.96	1.98	2.9	1520

The phase distribution of Ash 1 as function of temperature significantly differs for different atmospheres, as shown in Figure 13, where the reducing atmosphere is defined as a gas mixture of 60%CO–40%CO_2 while the oxidizing atmosphere is a gas mixture of 21%O_2–79%N_2, i.e. air.

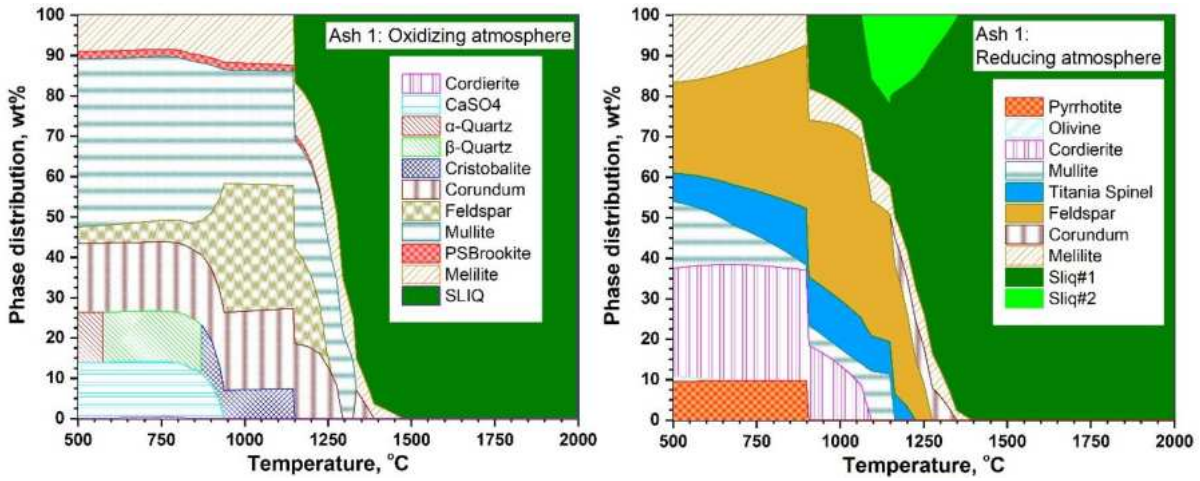

Figure 13: Phase distribution of Ash 1 at oxidizing (left) and reducing (right) atmosphere.

Comparing the experimentally measured AFT of Ash 1 of 1340 °C (see Table 1) with the temperature at which the ash is fully liquid under reducing conditions (1375 °C) in Figure 13 (left) it can be seen that the liquidus temperature is an excellent predictor for the experimentally measured flow temperature.

The mass fraction of a slag (between solidus and liquidus temperature) can also be used to evaluate the fouling behavior of fly ashes on surfaces of the downstream units of a gasifier or combustion chamber, and the description is reported elsewhere in detail, see [Kleinhans2018]. In addition to fly ash, trace elements released from fuels will also condense on these surfaces. The condensation mechanism of Zn vapor, taken as an example, can be illustrated using the Scheil-Gulliver cooling model [Zhao2021]. Figure 14 implies a supercooling of the condensate ZnO (a pure solid phase). The difference between the experimental and calculated $ZnCl_2$ condensate has been discussed in detail in [Zhao2021].

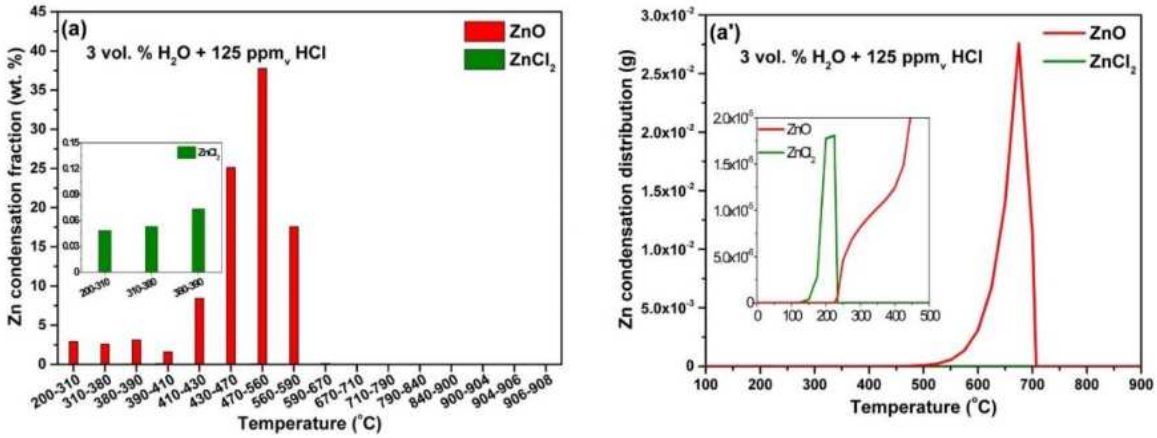

Figure 14: (a) IC and ICP-OES measurements for zinc-containing species under atmosphere containing HCl with 3 vol% steam compared to (a') the predictions with FactSage using the Scheil-Gulliver cooling model [Zhao2021] (Reprinted with permission by Elsevier).

References

[Wang2021] Hui Wang, Lihua Cheng, Jianglong Pu, Jigang Zhao, Melting Characteristics of Coal Ash and Properties of Fly Ash to Understand the Slag Formation in the Shell Gasifier, ACS Omega 24 (2021) 16066-16075.

[Kleinhans2018] Ulrich Kleinhans, Christoph Wieland, Flemming J. Frandsen, Hartmut Spliethoff, Ash formation and deposition in coal and biomass fired combustion systems: Progress and challenges in the field of ash particle sticking and rebound behavior, Progress in Energy and Combustion Science 68 (2018) 65-168.

[Zhao2021] Xin Zhao, Guixuan Wu, Jia Qi, Moritz to Baben, Michael Müller, Investigation on the condensation behavior of the trace element zinc in (Ar/H2O/HCl/H2S) gas mixtures and its practical implications in gasification-based processes for energy and power generation, Fuel 295 (2021) 120600.

Optimization of slag mobility in entrained flow gasifiers

In order to achieve smooth slag flow and tapping during the operation of entrained flow slagging gasifiers, a viscosity range ln(η, Pa·s) of 1.6–3.2 at 1400–1550 °C is desirable. Typically, blended feedstocks with the addition of fluxing agents are used to adjust the slag viscosity. As shown in Figure 15 (a), the viscosity of the model gasifier slags (for the composition see Table 2), taken as examples, is outside of the desirable viscosity range.

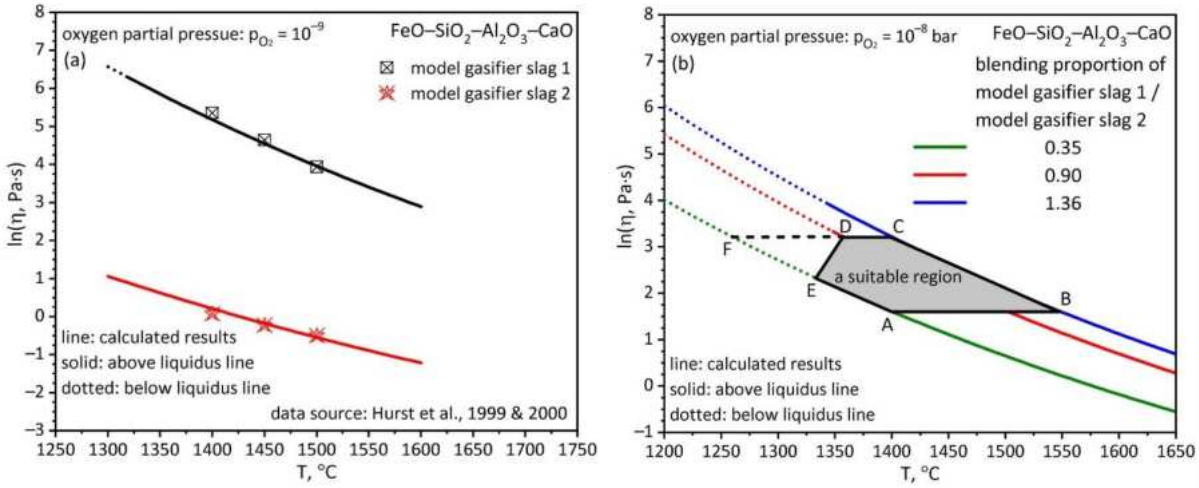

Figure 15: (a) Viscosity predictions compared to the experimental data [Hurst1999] [Hurst2000] of model gasifier slags at an oxygen partial pressure of 10^{-9} bar, (b) Selection of a suitable blending proportion of slags [Wu2021] (Reprinted with permission by Elsevier).

Table 2 Composition of the model gasifier slags in Figure 15 [Wu2019] (Reprinted with permission by Elsevier).

Model gasifier slag	Composition, mol%				$T_{liquidus}$, °C
	SiO_2	Al_2O_3	CaO	FeO	
1	68.61	13.84	12.59	4.96	1318
2	42.55	11.42	33.18	12.86	1245

Figure 15 (b) demonstrates desirable blending proportions of the selected slags as determined by the present viscosity model, where the oxygen partial pressure is assumed to be 10^{-8} bar, corresponding to a typical value during the operation of an entrained flow slagging gasifier. As a result, the gray area ABCDE in Figure 15 (b) indicates a suitable region of blending selected slags in combination with the liquidus information, i.e. the point E refers to a melting temperature of 1333 °C. It can be seen that the operating temperature can vary from 1333 °C to 1548 °C, and the blending proportion can vary from 0.35 to 1.36, where the blending proportion of 0.9 should result in an optimum viscosity of 15 Pa·s (i.e. ln(η, Pa·s) of 2.7) at 1400 °C. Information

regarding fluctuations of the operating temperature, slag composition, and atmosphere can be used to further determine an optimum blending proportion. For the determination of blending proportions of three or more slags, please see [Wu2019].

References

[Wu2019] Guixuan Wu, Sören Seebold, Elena Yazhenskikh, Joanne Tanner, Klaus Hack, Michael Müller, Slag mobility in entrained flow gasifiers optimized using a new reliable viscosity model of iron oxide containing multicomponent melts, Applied Energy 236 (2019) 837–849.

[Hurst1999] H.J. Hurst, F. Novak, J.H. Patterson, Viscosity measurements and empirical predictions for some model gasifier slags, Fuel 78 (1999) 439-444.

[Hurst2000] H.J Hurst, J.H Patterson, A Quintanar, Viscosity measurements and empirical predictions for some model gasifier slags-II, Fuel 79 (2000) 1797-1799.

Density Calculation for Specific Phases in Process Modelling

The knowledge of phase densities is essential for accurate process modelling, as it reveals critical insights into the separation and settling behaviour of complex multicomponent systems. Density-driven phase separation plays a key role across several metallurgical applications, including Cu-, Pb-, and Fe-metallurgy. With the latest GTOx version, users can now calculate the density of solid compounds as well as solid and liquid solutions, enabling both qualitative and quantitative descriptions of separation phenomena. This capability is demonstrated through a representative case study from the field of copper metallurgy.

Copper pyrometallurgy produces substantial amounts of converter slag and leaching residue, with conventional smelting slag containing up to 4.5 wt.% copper and 50 wt.% iron. Much of this slag, where copper is dispersed in complex, interlinked phases, is discarded in landfills, while less than 12% is recovered, leading to significant metal loss and environmental harm. To illustrate how density-driven separation can address this issue, the settling behaviour of matte and Cu-metal droplets during slag cleaning is examined using the study by Lan et al. [Lan2018] as a reference. In that work, a super-gravity separation method is proposed for Cu-Fe-Si-S-O slags, employing high-speed centrifugal force to rapidly and efficiently isolate metallic copper and an iron-rich (magnetite) phase at relatively low temperatures. By amplifying gravitational effects, this technique accelerates separation through density differences, while preserving the underlying separation mechanisms. This thorough experimental study provided compositions for each phase, which were needed for the density calculations based on GTOx.

The density calculation focused on the 1200 °C experiment, using the starting compositions from [Lan2018] detailed in Table 3. Within the crucible, the slag, matte, and Cu-metal phases were liquid and the magnetite phase (Fe_3O_4) was solid. The Cu-Fe-Si-S-O-rich slag, the major phase, was purified via centrifugal force, which accelerated phase separation without altering the underlying phenomena. Post-separation SEM and XRD analyses revealed that the slag contained only trace amounts of matte and magnetite. High-temperature microscopy of the metallic Cu phase confirmed it was free of matte or magnetite inclusions. Due to their lower densities compared to liquid Cu, matte and magnetite settled in a layer above the Cu metal. Consequently, the phase distribution in the crucible is arranged from top to bottom as follows: slag, a transitional mixed zone of matte and Fe_3O_4, and metallic Cu at the bottom, as illustrated in Figure 16.

The densities of multicomponent liquid phases calculated by GTOx were benchmarked against experimental values, showing mean deviations of 1.2% for the metallic melt, 2.3% for slag, and 4.3% for matte (see Figure 16). This confirms that GTOx achieves reliable accuracy across all liquid phases in this study. For the solid phase, the density of Fe_3O_4 (magnetite) was taken from pure compound data, yielding 5.10 g/cm^3. The densities for the liquid slag, matte, and copper melt were calculated as 3.61, 4.48, and 8.03 g/cm^3, respectively, based on their given chemical compositions in Table 3. These values accurately reflect the experimentally observed phase distribution in the crucible: a top layer of slag, a middle transitional zone containing matte and magnetite, and a bottom layer of pure metallic copper.

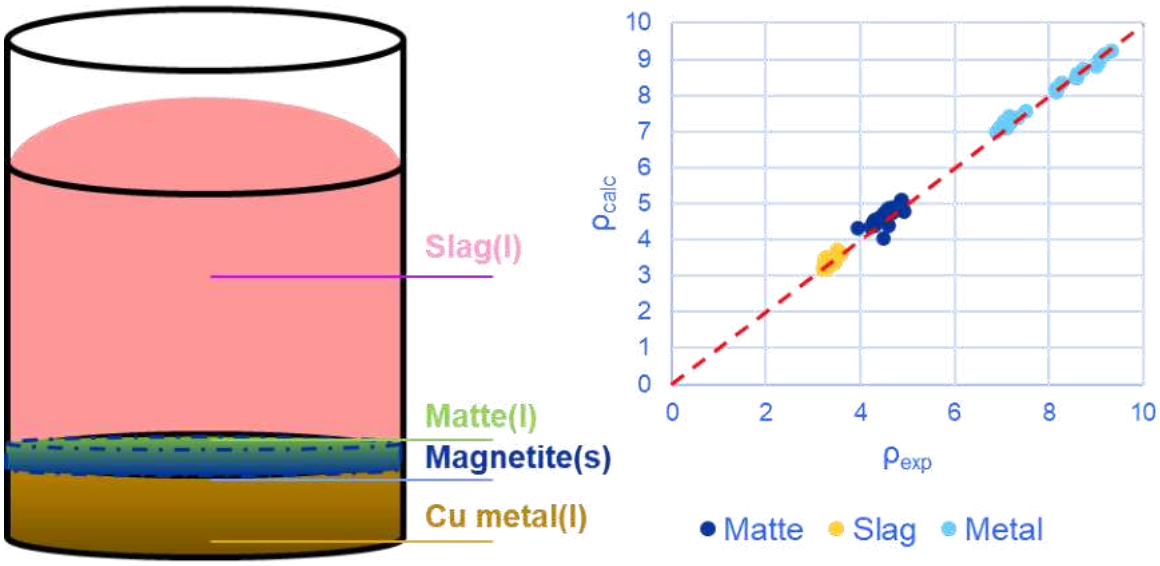

Figure 16: Schematic of the layers of different phases in the settling vessel at 1200 °C (left) and comparison of the benchmarked densities calculated with GTOx for the relevant types of liquid phases (right).

Until now, users had to rely on approximate phase densities, such as those for Cu-based matte and slags, sourced from general liquid data repositories. Based on the single liquid (SLiq) phase concept, which accounts for miscibility gaps, GTOx now enables calculation of precise densities for specific slag, matte, and metallic liquid compositions, representing a significant advancement. This approach provides the flexibility to compute density values tailored to any desired system.

As the initial slag is agitated, the droplets of matte and metal, as well as the solid magnetite particles, will settle towards the bottom of the crucible. The higher the agitation, the higher the settling rate will be. In a real process, it turns out, however, that settlement velocity is a function of the density difference between the individual phases. The higher the density difference between the droplet/particle relative to the slag (medium through which the particles settle down), the higher the settling rate will be. This can be expressed by the final settlement velocity of the droplet (v) which can be calculated using a special form of the Stokes equation, $v = \frac{g*D^2*(\rho_d-\rho_m)}{12\eta_m}$ as given by [Wang2023], where g is the acceleration constant of gravity, D is the droplet diameter, ρ_d and ρ_m are the densities of the droplet and the medium, and η_m is the viscosity of the medium. The resulting density differences for the phases obtained for the study [Lan2018] are given in Table 3**.**

Assuming that the particle sizes are approximately the same for all settling phases, the density differences relative to the medium, i.e. the slag, unequivocally indicate that the liquid metal droplets will have the largest settling velocity, which confirms the experimental findings of [Lan2018].

Table 3 Chemical compositions of the Cu-Fe-Si-O-S rich slag, Cu matte, Magnetite and metallic Cu at 1200 °C [Lan2018] and the calculated density values and density difference to the settling medium (slag) from the latest GTOx version.

	Composition, wt.%					Physical state at 1200 °C	**Density [GTOx]** (g/cm^3)	$\rho_{droplet} - \rho_{slag}$ (g/cm^3)
	Cu	Fe	Si	O	S			
Slag	0	52.84	15.74	31.42	0	Liquid	**3.6067**	**0**
Cu matte	38.64	32.9	0	0	28.45	Liquid	**4.4836**	**0.8769**
Magnetite	0	70.36	0	29.64	0	Solid	**5.1005**	**1.4938**
Metallic Cu	100	0	0	0	0	Liquid	**8.0330**	**4.4263**

Hence, it is evident that the Density model used in GTOx is well-suited for practical applications in Cu-metallurgy. With the latest version now supporting elements and relevant phases such as Pb, Fe, and Li, GTOx extends its applicability to a broad range of systems, including lead and iron metallurgy as well as lithium recycling. This allows users to obtain precise values for both density and settling velocity tailored to their specific multiphase compositions. The calculated settling velocity can be used to estimate the time required for various dispersed phases to settle through a given medium (in this case, slag). This estimation is valuable for determining the optimal dwell time before tapping during slag cleaning or separation processes.

To further enhance prediction accuracy, users can incorporate additional system-specific parameters, including furnace geometry, particle size distribution, and physical properties like viscosity. Hence, with GTOx, experimentally observed phenomena can be translated into quantitative insights, enabling precise analysis of complex phase behavior for advanced metallurgical process optimization.

References

[Lan2018] Xi Lan, Jintao Gao, Zili Huang, Zhancheng Guo, Rapid Separation of Copper Phase and Iron-Rich Phase from Copper Slag at Low Temperature in a Super-Gravity Field, Metallurgical And Materials Transactions B 49 (2018) 1165–1173. https://doi.org/10.1007/s11663-018-1235-6

[Wang2023] Qin-Meng Wang, Ming-Xing Huang, Shu-Yang Yan, Song-Song Wang, Qing-Hua Tian, Xue-Yi Guo, Hydrodynamic simulation of metal droplet settlement in molten slag, Transactions of Nonferrous Metals Society of China 33(4) (2023), 1244-1257, ISSN 1003-6326. https://doi.org/10.1016/S1003-6326(23)66179-5.

Assessment examples

In this section, a selected number of cases for characteristic thermodynamic assessments which form part of the GTOx database is presented.

$ZnO-P_2O_5$

Available experimental data was used for the generation of thermodynamic data for the system $ZnO-P_2O_5$. The model of non-ideal associated solutions was used to describe the liquid phase containing the following associates: $ZnO \cdot P_2O_5$, $2ZnO \cdot P_2O_5$ and $3ZnO \cdot P_2O_5$. Seven literature sources concerning phase equilibria and five references dealing with the internal structure of the liquid phase have been used to generate a consistent thermodynamic dataset for the system. Figure 17 shows the phase diagram and Figure 18 the phase-internal species distribution in the liquid phase as function of the mole fraction of ZnO calculated with the Gibbs energy dataset. Calculated associate species distribution in the liquid phase $ZnO-P_2O_5$ at 1000 °C is compared with available experimental data (NMR, EMF, Raman). The calculation is done for the middle temperature of the experimental ones which cover 900 °C, 1000 °C and 1100 °C. The calculated results show a very good representation for all temperatures. Also, the agreement between experimental and calculated phase boundaries in Figure 17 is very good.

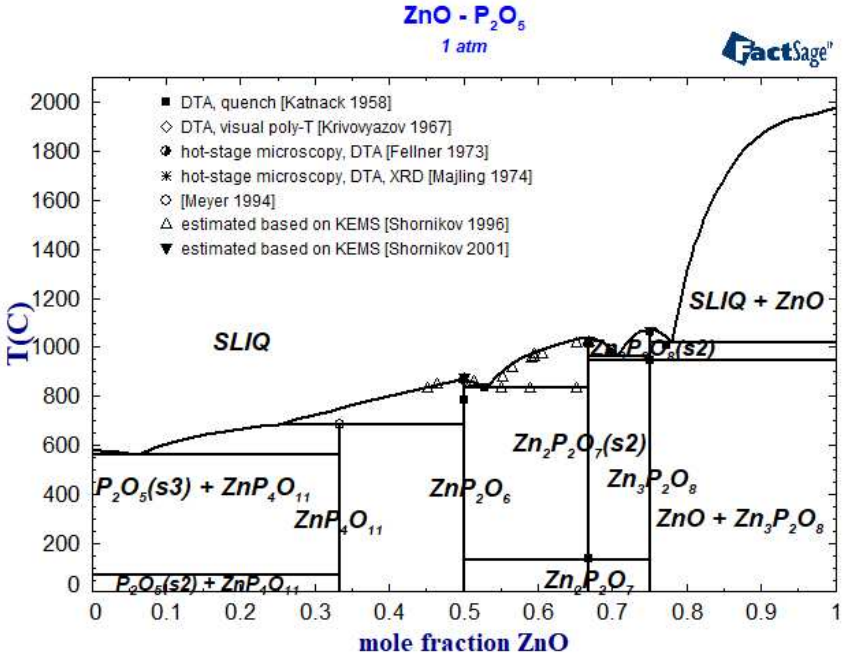

Figure 17: Calculated phase diagram of the system P_2O_5-ZnO compared with experimental data.

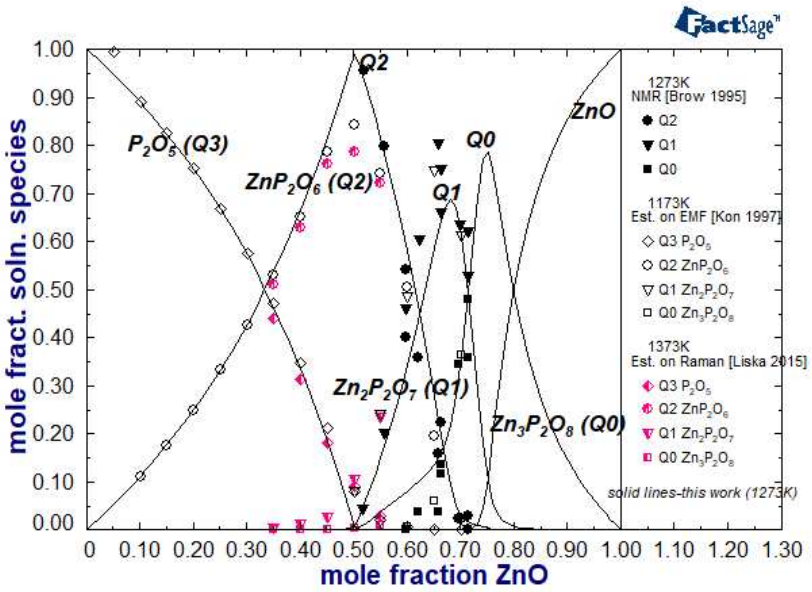

Figure 18: Calculated associate species distribution in the liquid phase P_2O_5-ZnO at 1000 °C compared with experimental data (NMR, EMF, Raman).

The experimentally observed structural units are considered as liquid constituents in the framework of the modified non-ideal associate species model. This fact indicates that the modified non-ideal associate species model is appropriate for the prediction of the structural features in the liquid phase with a direct link to, for example, the viscosity of the melt published by Wu et al. [Wu2019].

References

[Katnack1958] F.L. Katnack, F.A. Hummel, Phase Equilibria in the System ZnO-P_2O_5, J. Electrochem. Soc. 105 (3) (1958) 125-133.

[Shornikov1996] S.I. Shornikov, A.L. Shilov, M.M. Shultz, A mass spectrometric study of the thermodynamic properties of melts in the ZnO-P_2O_5 system, Zh. Phys. Khim. 70 (3) (1996) 485-491.

[Krivovyazov1967] E.L. Krivovyazov, K.K. Palkina, N.K. Voskresenskaya, Diagrammi plavkosti dvojnih sistem iz metafosfata zinka i metafosfatov Na ili K (in Engl. Melting diagram of the binary systems $Zn(PO_3)_2$-(Na or K)PO_3), Dokl. Akad. Nauk SSSr, Chemistry 174 (3) (1967) 610-613.

[Fellner1973] P. Fellner, J. Majling, Calculation of liquidus curves in phase diagrams $Na_4P_2O_7$-$Mg_2P_2O_7$ and $Na_4P_2O_7$-$Zn_2P_2O_7$, Chem. zvesti 27 (6) (1973) 728-731.

[Majling1974] J. Majling, S. Palco, F. Hanic, J. Petrovic, Phase equilibria in the system $Na_4P_2O_7$-$Zn_2P_2O_7$, Chem. zvesti 28 (3) (1974) 294-297.

[Meyer1994] K. Meyer, H. Hobert, A. Barz, D. Stachel, Infrared spectra and structure of various crystalline ultraphosphates and their glasses, Vibrational Spectroscopy 6 (3) (1994) 323-332.

[Shornikov2001] S.I. Shornikov, Vaporization processes and thermodynamic properties of zinc phosphates, Proc. Electrochemical Society 12 (2001) 316-321.

[SGPS] SGPS - SGTE Pure Substances database (v13.1) 2017.

[Konakov1997] V.G. Konakov, B.A. Shakhmatkin, M.M. Shultz, Thermodynamic properties of {xZnO+(1−x)P_2O_5}(l), J. Chem. Thermodynamics 29 (7) (1997) 785-795.

[Brow1995] R.K. Brow, D.R. Tallant, S.T. Myers, C.C. Phifer, The short-range structure of zinc polyphosphate glass, J. Non-Crystalline Solids 191 (1995) 45-55.

[Liška2015] M. Liška, M. Lissová, A. Plško, M. Chromčíková, T. Gavenda, J. Macháček, Thermodynamic model and Raman spectra of ZnO–P_2O_5 glasses, J. Therm. Anal. Calorim. 121 (1) (2015) 85-91.

[Wu2019] G. Wu, S. Seebold, E. Yazhenskikh, J. Tanner, K. Hack, M. Müller, Slag mobility in entrained flow gasifiers optimized using a new reliable viscosity model of iron oxide-containing multicomponent melts, Applied Energy, 236 (2019) 837-849.

CaO-ZnO-P_2O_5

The following ternary phases are included in the present database along with the Slag phase: the solid solutions based on $Ca_3P_2O_8$ (C3P-C2S, HT; C3P-alpha, MT; C3P-beta, LT) and on $Zn_3P_2O_8$ (Z3P-beta, HT; Z3P-alpha, LT) as well as the intermediate solid solution based on $CaZn_2P_2O_8$-HT (CZ2P-HT) according to [Kreidler1967, Carbajal2011]. The phase boundaries reported in these two sources have been used to optimize the parameters of the liquid phase as well as the various solid phases. The resulting phase diagrams are shown in Figure 19 and Figure 20. It should be noted that the system has been considered as fully water-free. Thus, the phase $Ca_4P_2O_9$ appears in the diagrams instead of HAp (HAp=hydroxyapatite $Ca_{10}(PO_4)_6(OH)_2$), which is observed experimentally due to water impurities.

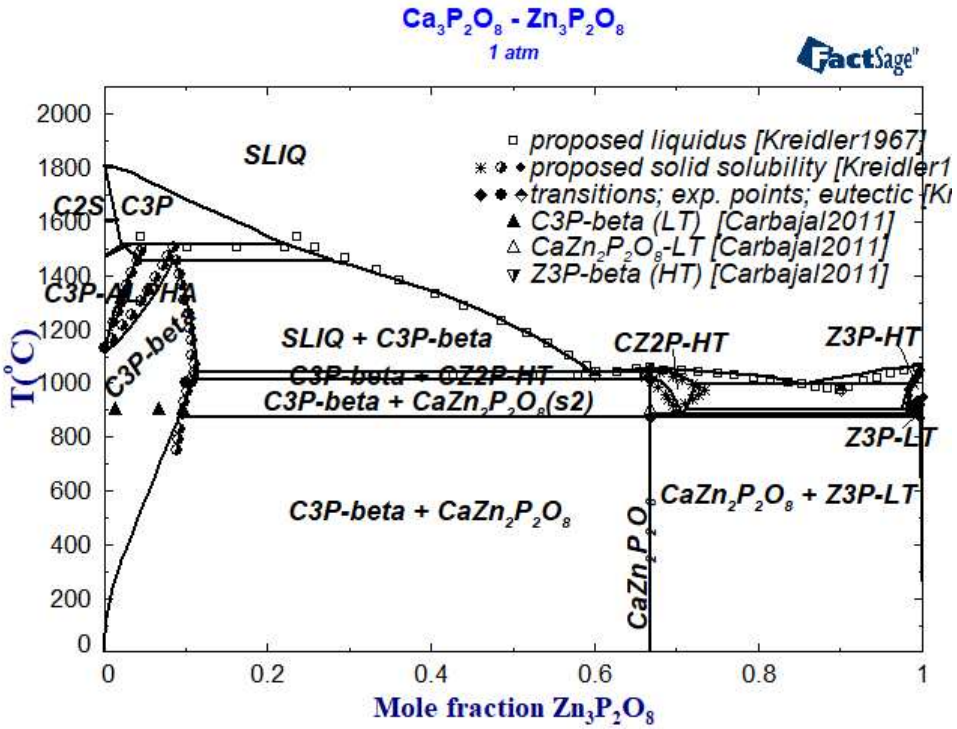

Figure 19: Calculated phase diagram of the system $Ca_3P_2O_8$-$Zn_3P_2O_8$ compared with experimental data [Kreidler1967, Carbajal2011].

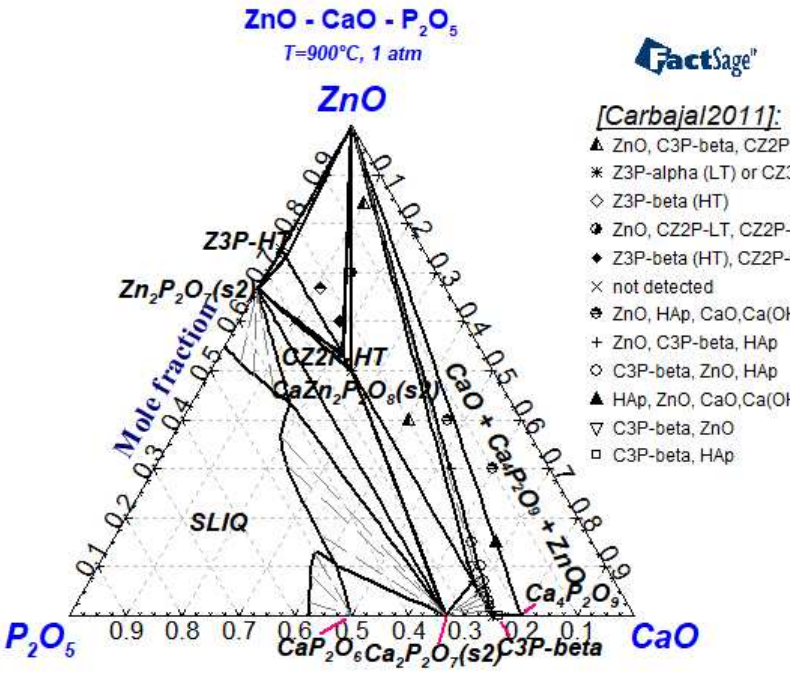

Figure 20: Calculated isothermal section at 900 °C in the ternary system CaO-P_2O_5-ZnO compared with experimental data [Carbajal2011].

References

[Kreidler1967] E.R. Kreidler, F.A. Hummel, Phase equilibriums in the System $Ca_3(PO_4)_2$-$Zn_3(PO_4)_2$, Inorg. Chem. 6 (3) (1967) 524-528.

[Carbajal2011] L. Carbajal, M.A. Sainz, S. Serena, A.C. Caballero, Á. Caballero, Solid-State Compatibility in Two Regions of the System ZnO–CaO–P_2O_5, Journal of the American Ceramic Society 94 (7) (2011) 2213-2219.

Al_2O_3-Li_2O-MgO

$MgAl_2O_4$ and $LiAl_5O_8$ (or $Li_{0.5}Al_{0.5}Al_2O_4$) form a complete spinel solid solution in the Li_2O-MgO-Al_2O_3 system [Menzheres1978, Izquierdo1980]. Spinels are oxides of the general type $A^TB^O{}_2O_4$ which have a very compact oxygen structure, with cations in tetrahedral (T) and octahedral (O) oxygen coordination. Simple examples are $MeO{\cdot}Me_2O_3$ which can be described with the formula $(Me^{2+})(Me^{3+})_2(O^{2-})_4$, where the divalent cations occupy the tetrahedral and the trivalent cations the octahedral sublattice sites. This makes it more obvious that the valence state of the metals plays an important part for the existence of this phase. $MgAl_2O_4$ has a normal spinel structure where Mg^{2+} is mostly placed on tetrahedral sites and Al^{3+} occupies octahedral sites. In the opposite system, $Li_{0.5}Al_{2.5}O_4$ has an inverse spinel structure where Al^{3+} combined with Li^{1+} are located on the octahedral sublattice, and Al^{3+} occupies the tetrahedral sublattice. Using a combined cationic species on the tetrahedral sublattice ($Li_{0.5}Al_{0.5}{}^{2+}$) deals with the charge compensation between the monovalent and the trivalent ion. The isothermal section for 1400 °C in the Al_2O_3-Li_2O-MgO system is presented in Figure **21** where $MgAl_2O_4$ and $LiAl_5O_8$ form a complete solid solution.

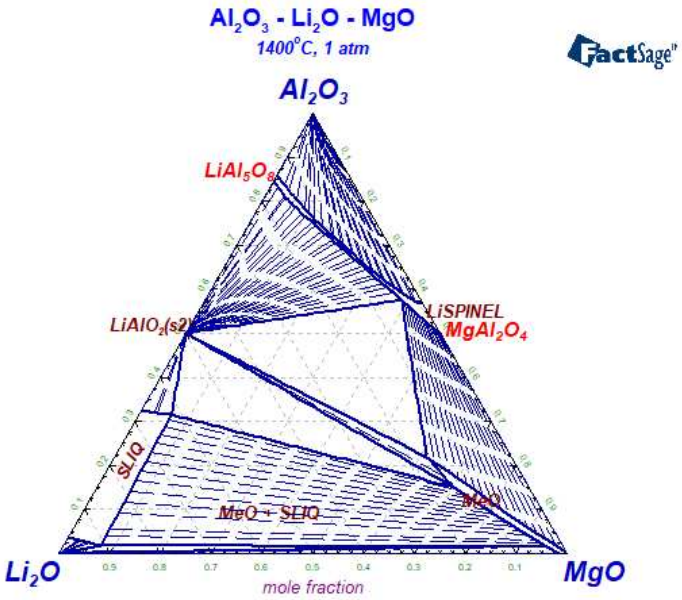

Figure 21: Isothermal section at 1400 °C in the Al_2O_3-Li_2O-MgO system.

References

[Mezheres1978] L. T. Menzheres, N. P. Kotsupalo, A. S. Berger, Zh. Neorg. Khim., 23 [10] 2804-2809 (1978).

[Izquierdo1980] G. Izquierdo, A. R. West, J. Am. Ceram. Soc., 63 [3-4] 227-227 (1980).

Viscosity modelling

Model parameters for the viscosity of oxide melts have been assessed, where available, by using the experimental data for pure oxides and selected binary and ternary systems. Great care has been taken to cover the well-known experimental facts by the modelling. These are: the lubricant effect, the weak lubricant effect, and the charge compensation effect. The following series of diagrams (Figure **22**) shows the successful use of the model for all these characteristic features.

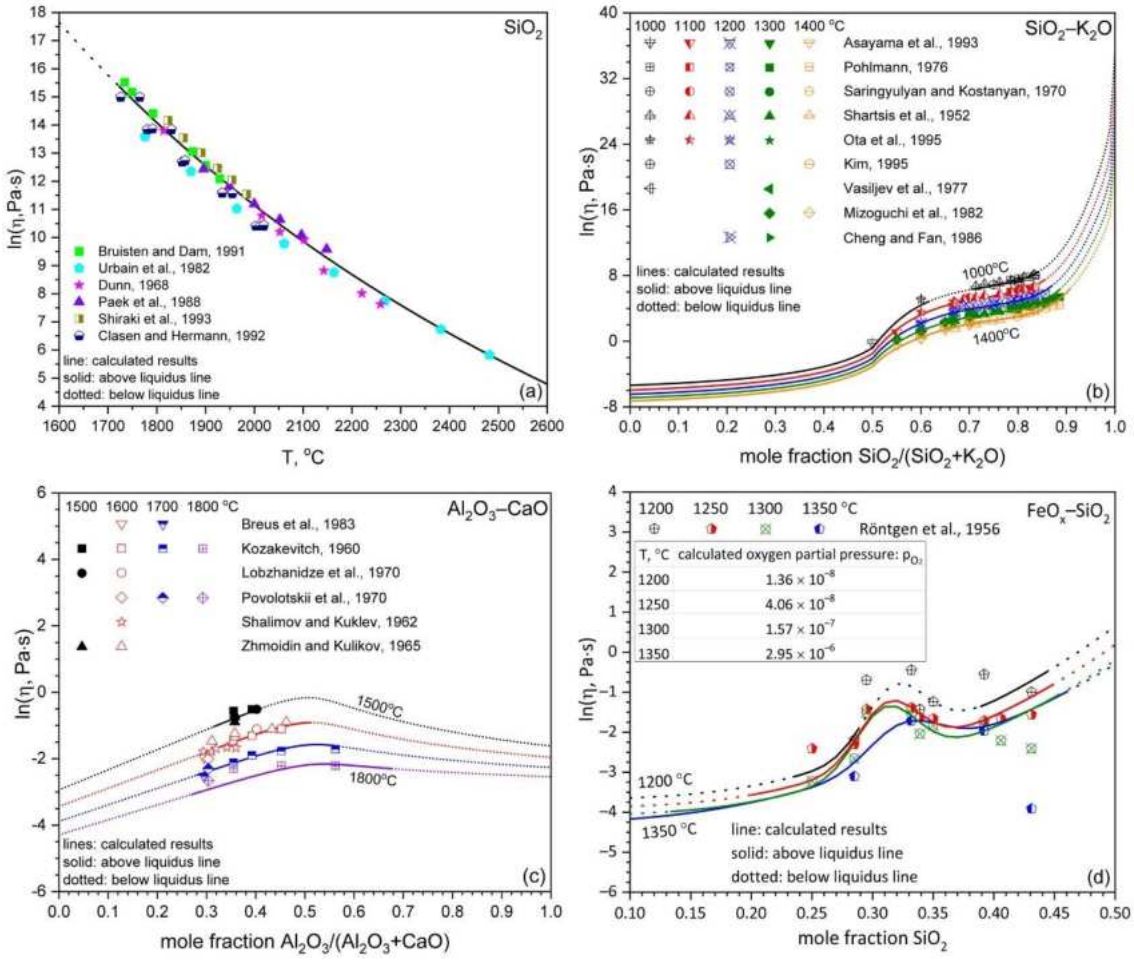

Figure 22: Comparison between experimental data and calculated data for the selected oxide melts SiO_2 (a), SiO_2-K_2O (b), Al_2O_3-CaO (c), and FeO_x-SiO_2 (d) [Wu2015,Part1] [Wu2018] (Reprint with permission by Elsevier).

For molten silica, the viscosity of more than 5 MPa·s (ln(η, Pa·s) ≈ 15.5) approaching the melting temperature is well reproduced by the present model, as shown in Figure 22 (a). It is seen from Figure 22 (b) that the viscosity decreases drastically when a small amount of a network modifier, here K_2O, is added into the pure silica melt, where the network modifier plays the role of a lubricant allowing silica clusters to glide more easily alongside each other ("*lubricant effect*"). Another clearly

noticeable but less strong decrease of the viscosity occurs around a SiO_2 mole fraction of 0.55 ("*weak lubricant effect*") due to possible ring structures. The present model can very well describe both these effects.

The present model also reproduces the viscosity maximum due to the "*charge compensation*" of Al_2O_3 with CaO, as shown in Figure 22 (c). The influence of the oxygen partial pressure on the viscosity behavior of systems containing multivalent iron oxide has also been considered. It is seen from Figure 22 (d) that a local viscosity maximum around the fayalite composition occurring in the binary system FeO-SiO_2 is described by the present model, where the position of the local viscosity maximum and its order of magnitude vary with temperature and oxygen partial pressure.

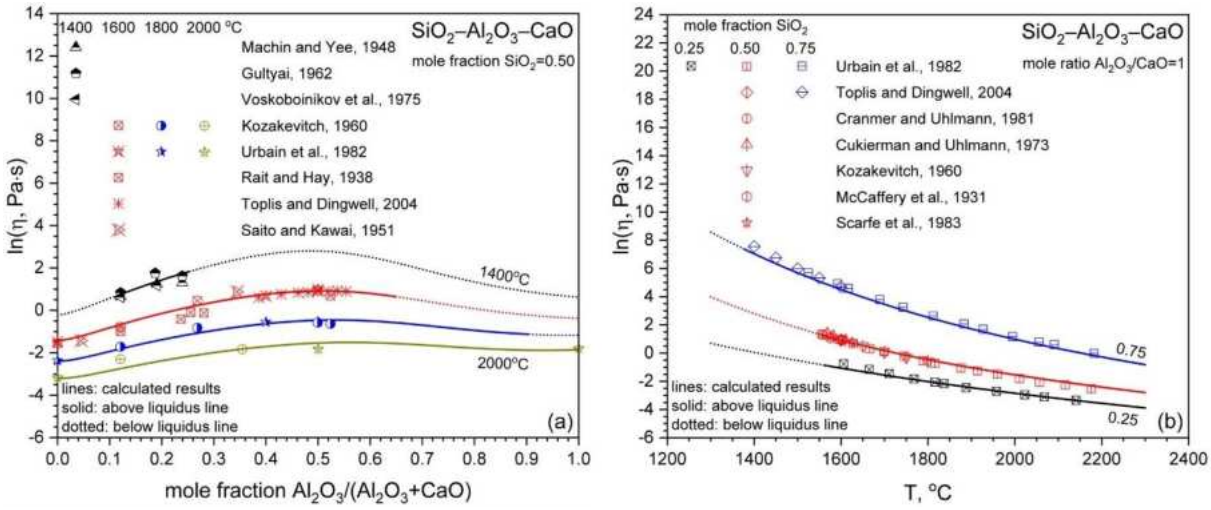

Figure 23: Comparison between experimental data and calculated data for the system SiO_2-Al_2O_3-CaO [Wu2015,Part2] (Reprinted with permission by Elsevier).

The extension of the model from low-order systems to high-order systems has been evaluated, as reported in detail elsewhere [Wu2015,Part2] [Wu2019] [Hack2019]. Figure 23 shows an example regarding the viscosity behavior induced by the charge compensation effect in the ternary system SiO_2-Al_2O_3-CaO. As shown in Figure 23 (a), the viscosity maximum is well described by the present model around the fully charge-compensated composition, which is $CaAl_2O_4$. The present model reproduces the order of magnitude of the viscosity maximum with increasing SiO_2 content. At the fully charge-compensated composition, the trend of the viscosity with temperature, as shown in Figure 23 (b), has also been well predicted. This indicates a good quality regarding the assessment of model parameters.

It is worth noting that the values of the model parameters are not just fitting parameters determined by minimization of the difference between experimental data and model calculations. They have a clear physical meaning, i.e. for each structural unit they represent the activation energy for viscous flow which increases as the ability of network formation rises. In addition, viscosities extrapolated to regions where no experimental data are available in literature have also been checked for reasonable behavior.

References

[Wu2015,Part1] Guixuan Wu, Elena Yazhenskikh, Klaus Hack, Erwin Wosch, Michael Müller, Viscosity Model for Oxide Melts Relevant to Fuel Slags. Part 1: Pure Oxides and Binary Systems in the System SiO_2–Al_2O_3–CaO–MgO–Na_2O–K_2O, Fuel Processing Technology 137 (2015) 93–103.

[Wu2018] Guixuan Wu, Sören Seebold, Elena Yazhenskikh, Klaus Hack, Michael Müller, Viscosity Model for Oxide Melts Relevant to Fuel Slags. Part 3: The Iron Oxide Containing Low Order Systems in The System SiO_2–Al_2O_3–CaO–MgO–Na_2O–K_2O–FeO–Fe_2O_3, Fuel Processing Technology 171 (2018) 339–349.

[Wu2015,Part2] Guixuan Wu, Elena Yazhenskikh, Klaus Hack, Michael Müller, Viscosity Model for Oxide Melts Relevant to Fuel Slags. Part 2: The System SiO_2–Al_2O_3–CaO–MgO–Na_2O–K_2O, Fuel Processing Technology 138 (2015) 520–533.

[Wu2019] Guixuan Wu, Sören Seebold, Elena Yazhenskikh, Joanne Tanner, Klaus Hack, Michael Müller, Slag mobility in entrained flow gasifiers optimized using a new reliable viscosity model of iron oxide containing multicomponent melts, Applied Energy 236 (2019) 837–849.

[Hack2019] Klaus Hack, Guixuan Wu, Elena Yazhenskikh, Tatjana Jantzen, Michael Müller, A CALPHAD approach to modelling of slag viscosities, Calphad 65 (2019) 101–110.

Density modelling

The model parameters have been assessed using the existing experimental data for pure oxides as well as binary and ternary subsystems. Due to a limited availability of experimental density data for pure oxides, the calculated densities by Ghiorso and Kress [Ghiorso2004] are used to derive the model parameters regarding the partial molar volume and partial molar thermal expansion.

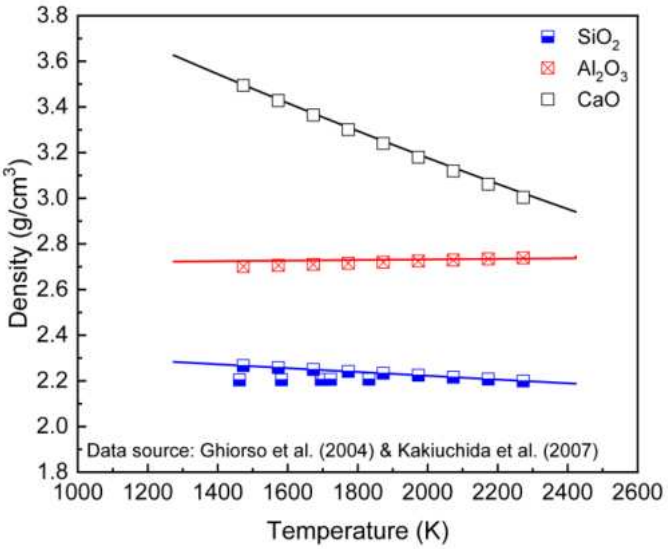

Figure 24: Comparison between the existing data [Ghiorso2004] [Kakiuchida2007] and model predictions for SiO_2, Al_2O_3 and CaO**.**

As shown in Figure 24, for SiO_2 and CaO the density usually decreases as temperature increases. However, the figure also shows that the density of Al_2O_3 increases slightly with increasing temperature. This unusual effect may be caused by the structural evolution of OAl_3 triclusters. As temperature increases, the stability of these triclusters decreases and the oxygen coordination number increases, which leads to a decrease in the molar volume of Al_2O_3. This structural variation with respect to the temperature requires a negative partial molar thermal expansivity of Al_2O_3.

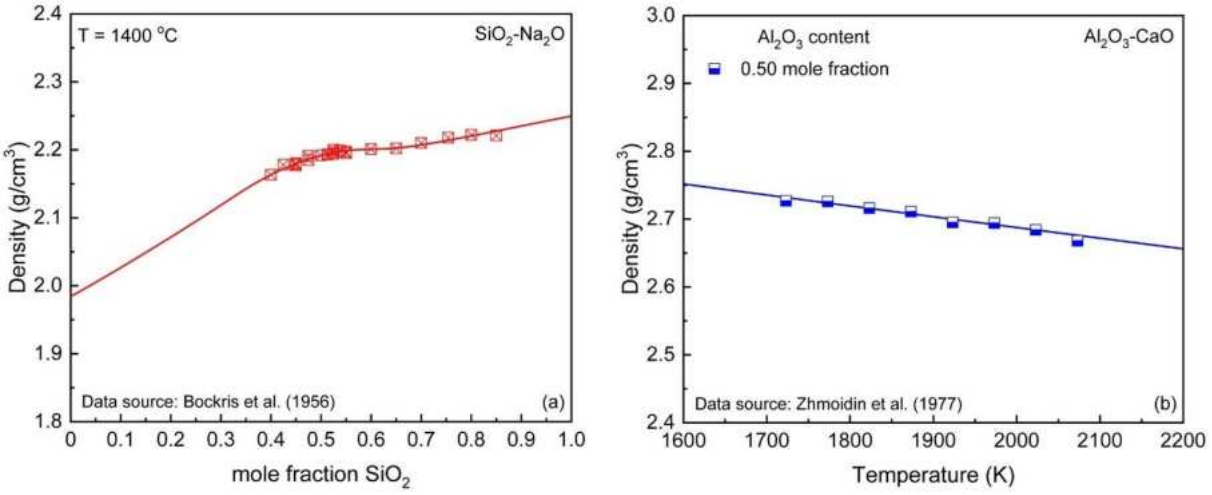

Figure 25: Comparison between the existing data [Bockris1956] [Zhmoidin1977] and model predictions for the binary systems SiO_2-Na_2O (a) and Al_2O_3-CaO (b)**.**

The experimental data of the binary system SiO_2-Na_2O are well reproduced by the present model, as shown in Figure 25 (a), where a small hump in density occurs probably due to the formation of a ring structure. Figure 25 (b) shows that the model predictions are in good agreement with the experimental data of the binary system Al_2O_3-CaO. It is seen that the density decreases with increasing temperature, where Al_2O_3 plays a different structural role compared to that in a pure Al_2O_3 melt, because Al_2O_3 is almost fully compensated by CaO, and the quasi-tetrahedron $CaAl_2O_4$, rather than the OAl_3 tricluster, is dominant.

When the model is extended to the ternary system SiO_2-Al_2O_3-CaO, the model predictions are consistent with the experimental density data, as shown in Figure 26. This indicates that the structural dependence of density has been well described by the present model regarding the Al_2O_3-induced charge compensation effect.

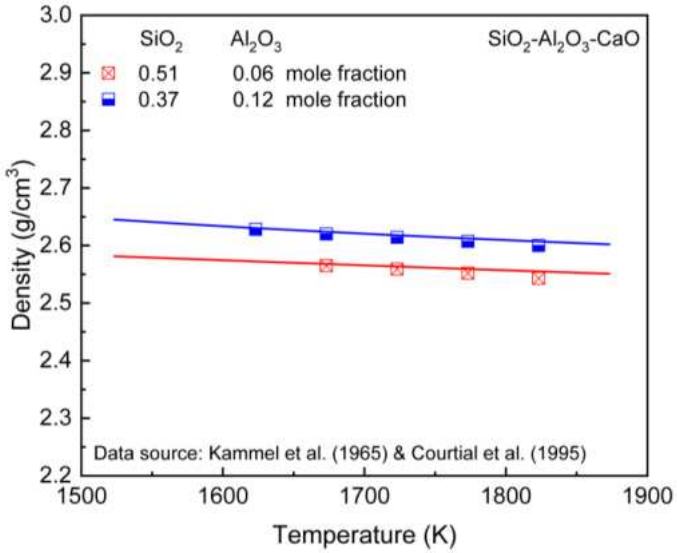

Figure 26: Comparison between the existing data [Kammel1965] [Courtial1995] and model predictions for the ternary system SiO_2-Al_2O_3-CaO.

References

[Ghiorso2004] M. Ghiorso, V.C. Kress, An equation of state for silicate melts. II. Calibration of volumetric properties at 10^5 Pa, Am. J. Sci. 304 (2004) 679-751.

[Kakiuchida2007] H. Kakiuchida, E.H. Sekiya, N. Shimodaira, K. Saito, A.J. Ikushima, Refractive index and density changes in silica glass by halogen doping, J. Non-Cryst. Solids 353 (2007) 568-572.

[Bockris1956] J. O'M. Bockris, J.W. Tomlinson, J.L. White, The structure of the liquid silicates: partial molar volumes and expansivities, Trans. Faraday Soc. 52 (1956) 299-310.

[Zhmoidin1977] G.I. Zhmoidin, G.S. Smirnov, V.N. Gladkii, Effect of atmospheric composition on the density of melts of the system CaO-Al_2O_3 (in Russian), Neorg. Mater. 13 (1977) 552-553.

[Kammel1965] R. Kammel, H. Winterhager, Struktur und Eigenschaften von Schlacken der Metallhuttenprozesse. V. Dichtebestimmungen und elektrische Leitfähigkeitsmessungen an Schmelzen des Systems Kalk-Tonerde-Kieselsaure, Erzmetall. 18 (1965) 9-17.

[Courtial1995] P. Courtial, D.B. Dingwell, Nonlinear composition dependence of molar volume of melts in the CaO-Al_2O_3-SiO_2 system, Geochim. Cosmochim. Acta 59 (1995) 3685-3695.

Database compatibility

GTOx version 19 can be used alone or together with many other databases available in FactSage:

- SGPS (complex gas phases or first-order approximation for any other substance)
- FactPS (complex gas phases or first-order approximation for any other substance) (slightly lower compatibility than with SGPS)
- aiMP / aiOQ (zeroth-order approximation for any other substances, lower compatibility but much larger material system covered)
- FSstel (steels, several superalloys)
- SpMCBN (non-oxide ceramics and refractory alloys)
- FTlite (light metals)
- FScopp (copper alloys)
- FSlead (lead alloys)
- SGTE solutions (general metal alloys, but data coverage for specific alloys is lower compared to the specialized databases indicated above)

Note: For any combinations that include FSstel, SpMCBN, FTlite, FScopp, FSlead, or SGTE Solutions, our recommendation is to utilize the liquid phase of that database and remove all pure metal endmembers from the SLIQ phase in GTOx using the " * - custom select end-members " option. Metallic solid solutions should be taken only from the respective alternative databases, not from GTOx. Please be aware that oxygen solubilities in liquid metal and solubilities of metallic components in the liquid Slag phase cannot be calculated with this approach.

We will be happy to assist you in the selection of databases, please contact us if you have any questions!

Phases

Unified Liquid phase (SLiq)

In contrast to older versions of the GTOx database the present version contains thermodynamic data for only one liquid phase. The reason for that is given by the fact that in real world systems there are many cases in which it is possible to change composition continuously from a liquid metal state to a molten oxide (Fe-O or Cu-O) or from a molten oxide to a matte (molten sulfide) (Cu-O-S). Even the transition from a molten silicate to a sulphatic melt can be found in reality (Mg_2SiO_4-$MgSO_4$). It was thus decided to integrate the separated liquids Slag, Sulphate and Metal, which have been so far part of the GTOx database, into one liquid. This is called "**SLiq**" indicating by the name that there is a **S**ingle **Liq**uid covering all possible liquid states with one dataset. It is obvious that for proper use of the SLiq phase the I- or even the J-option must be used to include the possible miscibility gaps into the calculations. For a detailed discussion of the new approach see the chapter "What is new in version 19?" below. The SLiq phase contains data for the following components:

Oxides	**Al_2O_3-CaO-CO_2-CoO-Co_3O_4-Cr_2O_3-CuO-Cu_2O-FeO-Fe_2O_3-Li_2O-MgO-MnO-Mn_2O_3-K_2O-Na_2O-NiO-P_2O_5-PbO-SO_3-SiO_2-SrO-TiO_2-Ti_2O_3-V_2O_3-V_2O_5-ZnO**
Metals	**Al, Ca, Co, Cr, Cu, Fe, Li, Mg, Mn, K, Na, Ni, Pb, Si, Sr, Ti, V, Zn + C, P, S, O**
Phosphates	**of the metals Ca, Co, Cu, Fe, Mg, Mn, Pb, Sr, Zn**
Sulfides	**of the metals Al, Ca, Co, Cr, Cu, Fe, Li, Mg, Mn, K, Na, Ni, Pb, Si, Sr, Ti, Zn**
Sulfates	**of the metals Ca, K, Mg, Na, Ni, Pb and Pyrosulfates of the metals K, Na**
Carbonates	**of the metals Ca, K, Mg, Na**
Chlorides	**of the metals Ca, K, Mg, Na**
Fluorides	**of the metals Al, Ca, Mg**

With the new set of constituents it is possible to calculate even binary metal-oxygen or metal-sulphur systems. All phase diagrams are available in a separate PDF document which is provided by GTT on request.

Solid solution phases

The GTOx database contains **183 solid solution phases**. The complete list including a short description for each phase can be provided upon request.

Solid stoichiometric compounds

The GTOx database includes **1366 stoichiometric compounds**. The complete list can be provided upon request.

References

[Hack2012] Hack K., Jantzen T., Müller M., Yazhenskikh E., Wu G. A novel thermodynamic database for slag systems and refractory materials // Proceedings of the 5th Int. Congress on the Science and Technology of Steelmaking. ICS (2012). Dresden. Germany.

[Yazhenskikh2014] Yazhenskikh E., Jantzen T., Hack K., Müller M. Critical thermodynamic evaluation of oxide system relevant to fuel ashes and slags: Potassium oxidemagnesium oxidesilica, Calphad 47 (2014), 35–49

[Jantzen2016] Jantzen T., Hack K., Yazhenskikh E., Müller M. Evaluation of thermodynamic data and phase equilibria in the system Ca–Cr–Cu–Fe–Mg–Mn–S: Part I: Binary and quasibinary subsystems, Calphad 56 (2016), 270–285; Part II: Ternary and quasiternary subsystems, Calphad 56 (2017), 286–302.

[Besmann2002] Besmann T.M., Spear K.E. Thermodynamic modelling of oxide glasses, J. Am. Ceram. Soc. 85 (2002), 2887–2894.

[Wu2018] Wu G., Seebold S., Yazhenskikh E., Hack K., Müller M. Viscosity model for oxide melts relevant to fuel slags. Part 3: The iron oxide containing low order systems in the system SiO_2–Al_2O_3–CaO–MgO–Na_2O–K_2O–FeO–Fe_2O_3, Fuel Processing Technology 171 (2018), 339–349.

[Jantzen2017] T. Jantzen, K. Hack, E. Yazhenskikh, M. Müller, Evaluation of thermodynamic data and phase equilibria in the system Ca–Cr–Cu–Fe–Mg–Mn–S part I: Binary and quasi-binary subsystems, Calphad 56 (2017) 270-285.

[Jantzen2017-2] T. Jantzen, K. Hack, E. Yazhenskikh, M. Müller, Evaluation of thermodynamic data and phase equilibria in the system Ca-Cr-Cu-Fe-Mg-Mn-S Part II: Ternary and quasi-ternary subsystems, Calphad 56 (2017) 286-302.

What is new in version 19?

The current update is important for two major reasons:

- Unification of the data for the liquid phase
- Addition of new and reassessed subsystems
- Addition of ML-informed density estimations for solid compounds, solutions and the multicomponent liquid phases

Unification of the data for the liquid phase

The following diagrams illustrate the need for a unified thermodynamic treatment of the liquid state. Figure 27 shows that the miscibility gap in the Fe-O system closes at higher temperatures and this requires a single liquid to be described.

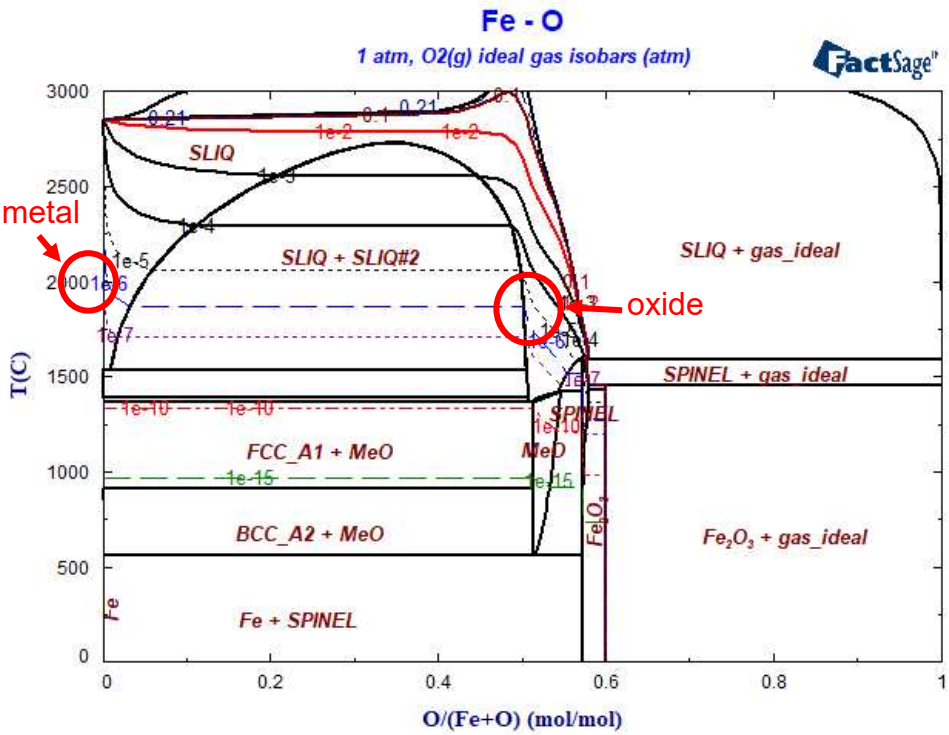

Figure 27: The Fe-O-Phase diagram.

Figure 28 shows by way of the isothermal section of the Fe-O-S system that there is need for a unified description of a liquid state which covers metallic, oxidic as well as sulphidic compositions. There is a miscibility gap on the Fe-O edge which extends into the ternary while on the Fe-S edge a metallic liquid begins in the Fe-rich corner and protrudes into the Fe-S binary. On the other hand, it is possible to combine molten “FeS” with molten “FeO” without any demixing.

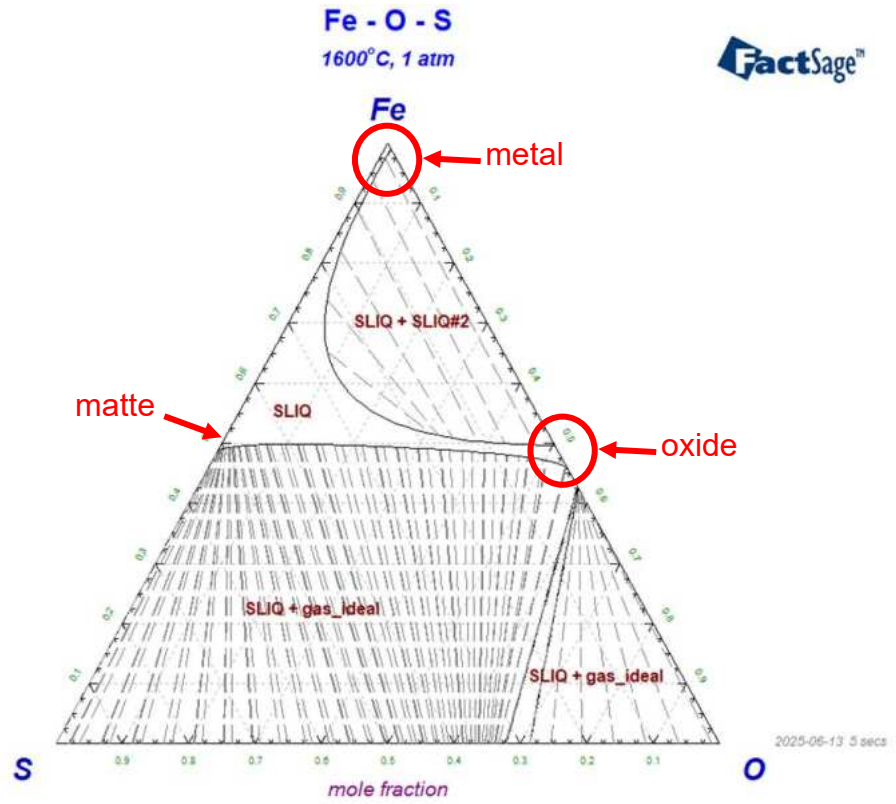

Figure 28: The isothermal section of the system Fe-O-S at T=1600°C.

Figure 29 depicts the continuous transition from a sulphate to a sulfide melt for the system K_2S-K_2SO_4.

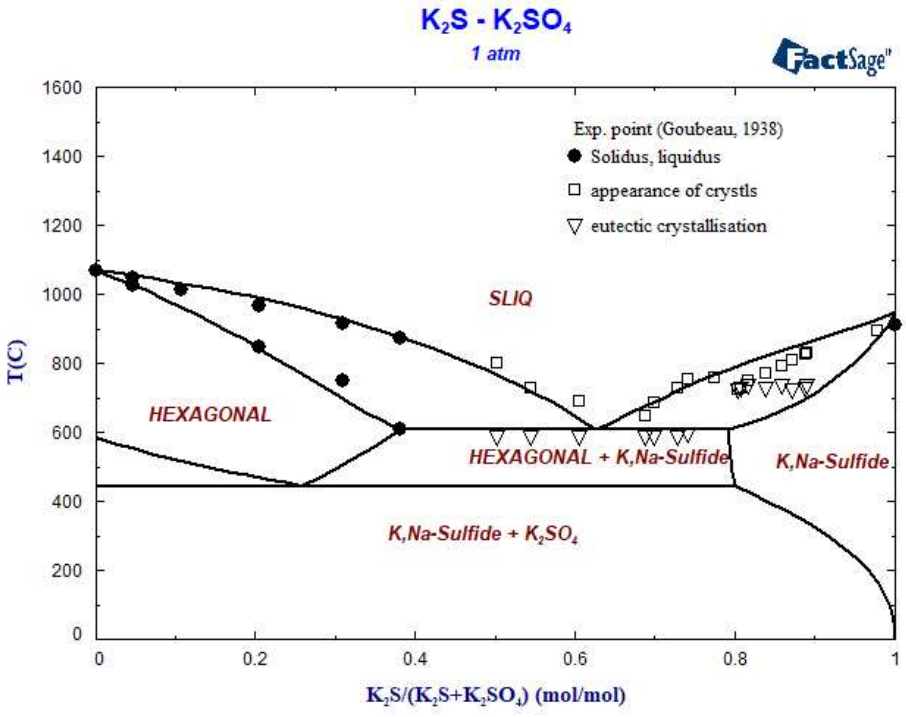

Figure 29: Phase diagram for the system K_2S-K_2SO_4.

In addition to the three phase diagrams shown above, which have all been calculated with the new dataset “SLiq” for the unified liquid phase, below are given some further highlights of the successful unification of the data for the generalized liquid phase.

Figure 30 shows the Fe-rich corner of the Fe-Cr-O system at T=1600 °C. It is worth noticing that the melt from which the different Cr_2O_3-based solids precipitate is molten iron with small amounts of dissolved oxygen as well as chromium. Molten “slag” is not involved.

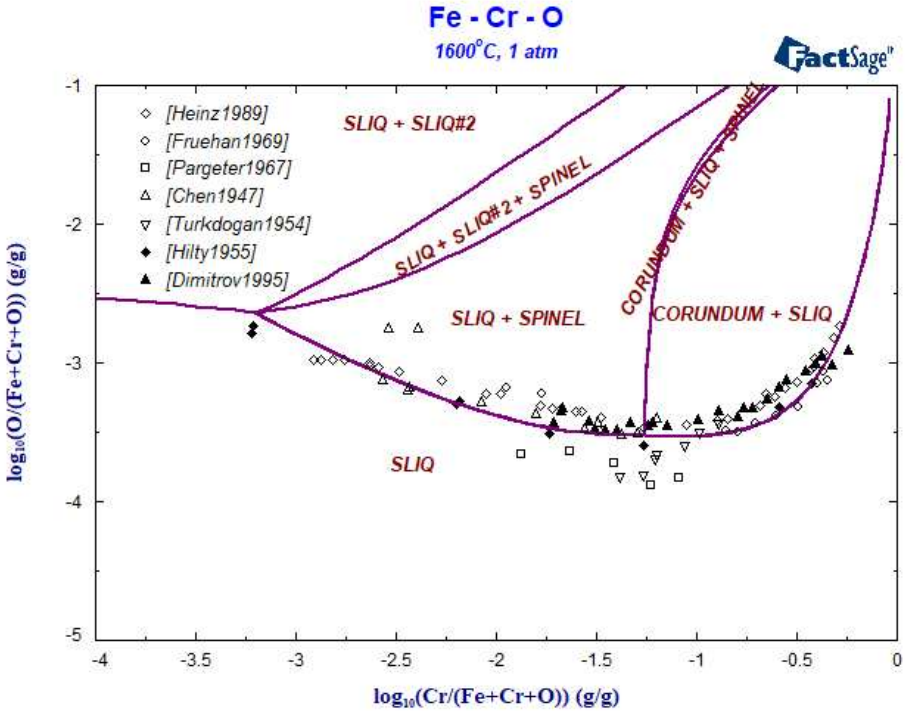

Figure 30: The precipitation range for Fe-rich melts in the Fe-Cr-O system.

Similarly, Figure 31 and Figure 32 show the Fe-rich corners of the Fe-Ti-O and Fe-V-O system in which also different precipitate phases contribute to the respective solubility limits. The agreement with the experimental information is very good. In all cases a new associate of the type Fe_2MeO_4 (Me=Al, Cr, Ti, V…) had to be introduced to handle the localized interactions between Fe, the respective metal and oxygen in the very Fe-rich composition range. One particular feature common to all three diagrams (Figure 30 to Figure **32**) is especially worth noting: For very low contents of the metal component, all three systems exhibit a miscibility gap (SLIQ + SLIQ#2) which is fully consistent with the behavior of the Fe-O binary subsystem: At 1600°C liquid metal is in equilibrium with the liquid oxide phase. The respective metal component is dissolved in both liquids.

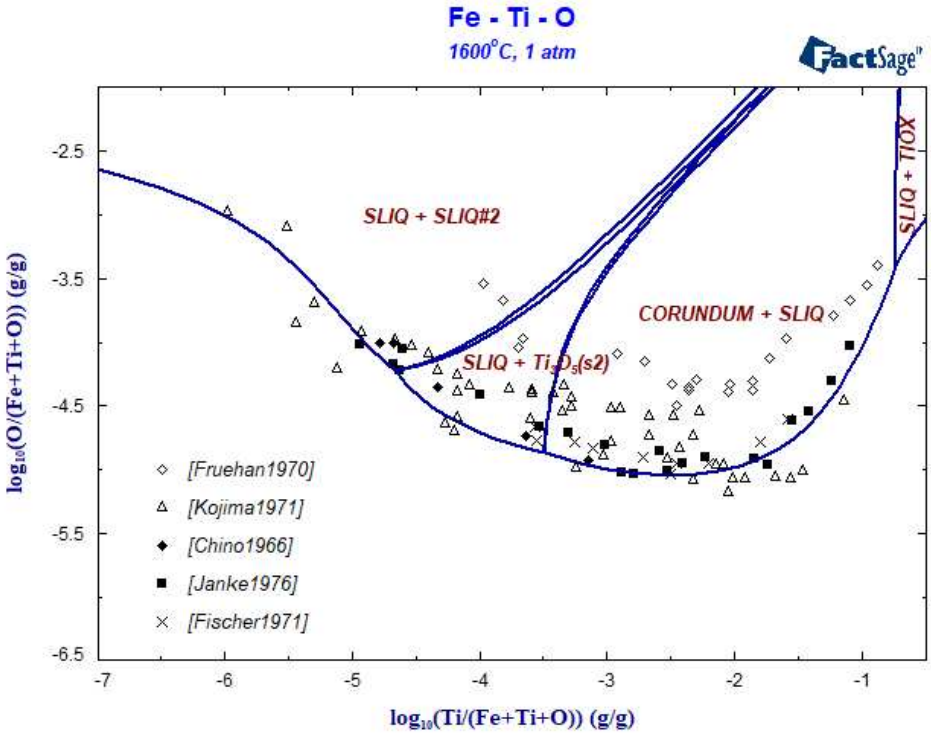

Figure 31: The precipitation range for Fe-rich melts in the Fe-Ti-O system.

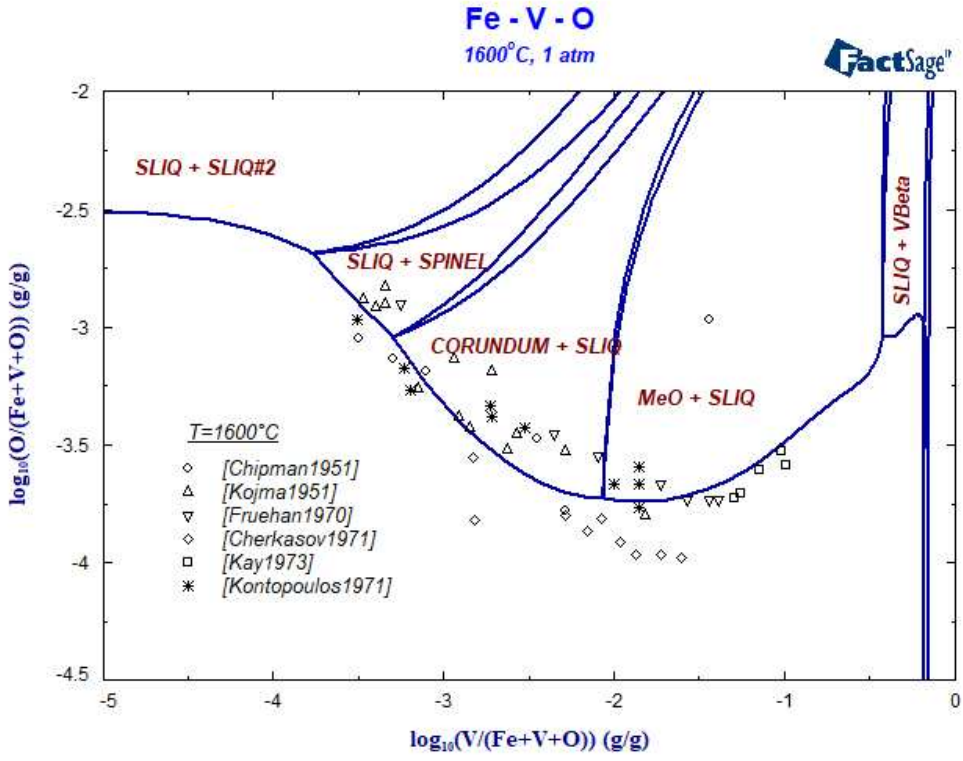

Figure 32: The precipitation range for Fe-rich melts in the Fe-V-O system.

An extreme case with threefold demixing is given in Figure 33. The system is FeO-SiO_2-P_2O_5 in contact with Fe. Because of the temperature (1600 °C) iron is liquid. Thus, a metallic melt (with solubility for Ca, Si, O and P) will be in contact with the solid

and/or liquid phases in the oxide subsystem (FeO-CaO-SiO_2). Since at certain compositions in the oxide subsystem there is demixing in the liquid slag in total three liquid phases can be in equilibrium.

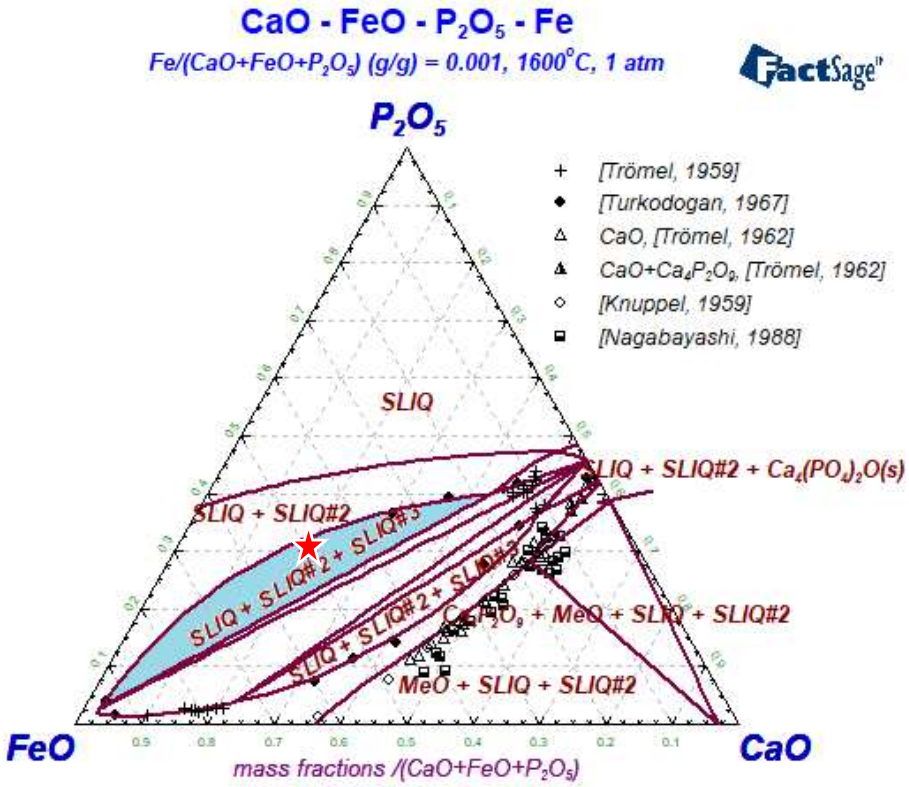

Figure 33: Threefold demixing in the system CaO-FeO-SiO2-Fe at 1600°C.

The following Figure 34 shows in tabular form the compositions of the three different liquids for the overall composition as marked with ★ in the liquid three phase region (Figure 33). One P_2O_5-rich and one FeO-rich oxide melt as well as an Fe-based liquid can easily be identified.

Figure 34: Tabular output of the composition of the three-melt equilibrium calculated for the overall composition marked with ★ in Figure 33.

A list of all new systems is provided below

Binary and Quasi-binary systems

New Binary Systems			New Quasi-binary Systems		
Al-Ca	Al-Co	Al-Cr	Al_2O_3-CoO-O_2	Al_2O_3-PbO	$CaCl_2$-CaO
Al-Cu	Al-Fe	Al-K	$CaCl_2$-$CaCO_3$	$CaCl_2$-$CaSO_4$	$CaCl_2$-K_2SO_4
Al-Li	Al-Mg	Al-Mn	$CaCl_2$-$MgCl_2$	$CaCl_2$-MgO	CaCl-Na_2SO_4
Al-Na	Al-Ni	Al-P	$CaCO_3$-$Na_2Co_3Cl_2$	$CaCO_3$-NaCl	CaCO-$CaCl_2$
Al-Pb	Al-Sr	Al-Ti	CaO-CoO-O_2	CaO-PbO	$CaSO_4$-KCl
Al-V	Al-Zn	Ca-Co	$CaSO_4$-NaCl	Co_3O_4-Cr_3O_4-O_2	Co_3O_4-Fe_3O_4-O_2
Ca-Cr	Ca-Cu	Ca-K	$Co3O_4$-Mn_3O4-O_2	CoO-CuO	CoO-FeO
Ca-Li	Ca-Mn	Ca-Na	CoO-K_2O	CoO-Li_2O	CoO-MgO
Ca-Ni	Ca-P	Ca-Sr	CoO-MnO	CoO-Na_2O	CoO-NiO
Ca-Ti	Ca-V	Ca-Zn	CoO-P_2O_5	CoO-PbO	CoO-SiO_2
Co-Cu	Co-Fe	Co-Li	CoO-SrO	CoO-TiO_2	CoO-V_2O_5
Co-Mg	Co-Mn	Co-Ni	CoO-ZnO	CoS-CrS	CoS-Cu_2S
Co-P	Co-Pb	Co-Si	CoS-FeS	CoS-MnS	CoS-NiS
Co-Ti	Co-V	Co-Zn	CoS-ZnS	Cr_2O_3-PbO	Cu_2O-PbO
Cr-Co	Cr-Fe	Cr-K	Cu_2S-PbS	CuO-PbO	Fe_2O_3-PbO
Cr-Li	Cr-Mn	Cr-Ni	$FeSO_4$-$PbSO_4$	FeS-PbS	K_2O-PbO
Cr-P	Cr-Pb	Cr-Si	K_2SO_4-NaCl	KCl-$K_2P_2O_7$	KCl-K_2SO_4
Cu-Cr	Cu-K	Cu-Li	KCl-K_3PO_4	KCl-KPO_3	KCl-Na_2SO_4
Cu-Mg	Cu-Mn	Cu-P	Li_2O-PbO	MgO-PbO	Mn_2O_3-PbO
Cu-Pb	Cu-Si	Cu-Sr	MnO-PbO	Na_2O-NaCl	Na_2O-PbO
Cu-Ti	Cu-V	Cu-Zn	NaCl-$Na_2P_2O_7$	NaCl-Na_2SiO_3	NaCl-Na_2SO_4
Fe-Ca	Fe-K	Fe-Li	NaCl-Na_3PO_4	NaCl-$NaPO_3$	NiO-PbO
Fe-Mg	Fe-Mn	Fe-Na	PbO-P_2O_5	PbO-$PbSO_4$	PbO-SiO_2
Fe-Ni	Fe-Pb	Fe-Si	PbO-SrO	PbO-TiO_2	PbO-V_2O_5
Fe-Sr	Fe-Ti	Fe-V	PbO-ZnO	PbS-$PbSO_4$	PbS-ZnS
K-Co	K-Li	K-Mn			
K-Pb	K-S	K-Sr			
K-Ti	K-V	K-Zn			
Li-Mn	Li-Pb	Li-S			
Li-Si	Li-Sr	Li-Ti			
Li-V	Li-Zn	Mg-Cr			
Mg-K	Mg-Li	Mg-Mn			
Mg-Na	Mg-Ni	Mg-P			
Mg-Pb	Mg-Si	Mg-Sr			
Mg-Ti	Mg-V	Mg-Zn			
Mn-Ni	Mn-P	Mn-Pb			
Mn-Si	Mn-Sr	Mn-V			
Na-Co	Na-Cr	Na-Cu			
Na-K	Na-Li	Na-Mn			
Na-Pb	Na-Si	Na-Sr			
Na-Ti	Na-V	Na-Zn			
Ni-Cu	Ni-K	Ni-Li			

New Binary Systems			New Quasi-binary Systems		
Ni-Mn	Ni-Na	Ni-P			
Ni-Pb	Ni-Si	Ni-Ti			
Ni-Zn	Pb-Ca	Pb-Si			
Pb-Zn	P-Si	Si-Sr			
Si-Ti	Si-V	Si-Zn			
Sr-Co	Sr-Ni	Sr-Pbi			
Sr-Ti	Sr-V	Ti-P			
Ti-Zn	Zn-Cr	Zn-P			
Zn-Sr	Zn-V				

Ternary and Quasi-ternary systems

New Ternary Systems		
Al-Co-O	Ca-Co-O	Co-Cr-S
Co-Cu-O	Co-Cu-S	Co-Fe-O
Co-Fe-S	Co-K-O	Co-Li-O
Co-Mg-O	Co-Mn-O	Co-Mn-S
Co-Na-O	Co-Ni-O	Co-Ni-S
Co-Pb-O	Co-P-O	Co-Si-O
Co-Sr-O	Co-Ti-O	Co-V-O
Co-Zn-O	Co-Zn-S	Cr-Co-O
Cr-Pb-O	Cu-Pb-O	Cu-Pb-S
Fe-Pb-O	Fe-Pb-S	Mn-Pb-O
Pb-O-S	Pb-Sr-O	Pb-Zn-S
New Quasi-ternary Systems		
Al_2O_3-CaO-CoO	Al_2O_3-Co_3O_4-MgO	Al_2O_3-Co_3O_4-SiO_2
Al_2O_3-K_2O-P_2O_5	Al_2O_3-Na_2O-P_2O_5	Al_2O_3-PbO-SiO_2
Al_2O_3-PbO-TiO_2	CaO-Co_3O_4-SiO_2-O_2	CaO-CuO-PbO
CaO-Fe_2O_3-PbO	CaO-PbO-SiO_2	CaO-PbO-SrO
Co_3O_4-Li_2O-Mn_2O_3	CoO-Fe_2O_3-Mn_2O_3-O_2	CoO-Fe_3O_4-SiO_2-O_2
CoO-Li_2O-NiO	CoO-MgO-SiO_2	CoO-Mn_2O_3-TiO_2
CoO-MnO-SiO_2	CoO-NiO-SiO_2	Cu_2O-PbO-SiO_2
CuO-PbO-SrO	Fe_2O_3-K_2O-P_2O_5	Fe_2O_3-Na_2O-P_2O_5
Fe_2O_3-PbO-SiO_2	MgO-PbO-SiO_2	Na_2O-PbO-P_2O_5
Na_2O-PbO-SiO_2	NiO-PbO-TiO_2	PbO-P_2O_5-V_2O_5
PbO-SiO_2-ZnO	PbO-SrO-SiO_2	

Contact

In case of questions or to provide feedback, please open a new ticket in our support center: https://support.gtt-technologies.de/ or contact us via

GTT-Technologies
Kaiserstraße 103
52134 Herzogenrath, Germany
Phone: +49-(0)2407-59533
Fax: +49-(0)2407-59661
E-mail: info@gtt-technologies.de